Tectonophysics 786 (2020) 228460

Contents lists available at ScienceDirect

Tectonophysics

journal homepage: www.elsevier.com/locate/tecto

A geometric model to estimate slip rates from terrace rotation above an offshore, listric thrust fault, Kaikōura, New Zealand

Brendan Duffy

School of Earth Sciences, The University of Melbourne, Parkville, 3010, Melbourne, Australia

ARTICLE INFO

Keywords:
Kaikoura
Marine terrace uplift
Paleoseismic
Listric thrust fault
Quaternary
MIS 3 sea level

ABSTRACT

The Kaikōura Peninsula lies at the transition from subduction to continental collision at the southern end of the Hikurangi subduction system. This study uses a 2012 lidar survey over the Kaikōura Peninsula to re-map a flight of four uplifted Late Pleistocene marine terraces at high resolution. The lidar shows that the terraces are being progressively tilted landwards in a manner consistent with listric thrust faulting offshore. The fault, known as the Kaikōura Peninsula Fault, dips shallowly at c.30° to the northwest at depth and probably truncates the Seaward segment of the Hope Fault in the footwall of the Jordan Thrust. Geometric analysis of the tilt, using ages based on previous dating and a regional sea level curve, suggests that slip rates on the Kaikōura Peninsula Fault have ranged between 2.3 ± 1.5 mm/yr and 4.1 ± 1.3 mm/yr over the Late Pleistocene. The elevations of Late Holocene fringing beaches track regional sea level changes, apart from a departure indicating a single uplift event (penultimate earthquake) in the late 18th to earliest 19th century (1702–1838 CE), followed by uplift in the 2016 Kaikōura earthquake. The slip rate calculated from beach uplift, including the Kaikōura earthquake, is consistent with longer term rates. The accumulation of the slip over only c.220 years following > 2000 years of quiescence suggests that the offshore thrust and associated faults exhibit clustered behavior, possibly as a result of keystone faulting.

1. Introduction

Determining slip rates and understanding their temporal evolution, both on single faults and on fault systems, are important components of seismic hazard analysis, providing information on how faults are loaded in time and space (e.g., Knuepfer, 1992; Nicol et al., 2006; Dolan et al., 2007; Mouslopoulou et al., 2009). Derivation of these data requires knowledge of both the amount of slip and the age of a given displaced marker. Difficulties arise when a displaced marker's age is uncertain and its displacement cannot be directly measured. A common example of such a situation is provided by Quaternary terraces that have been uplifted above offshore thrust fault systems along convergent plate boundaries. In these settings, the ages of particular levels within a flight of uplifted terraces may be constrained by direct dating and correlation with sea-level curves. These data are then used to estimate the uplift rate (e.g. Muhs et al., 1992; Ota et al., 1996; Harris, 2011); however, (i) the underlying slip rates remain unknown, (ii) the uplift rate may vary significantly away from the site for which it is determined and (iii) the accuracy of uplift rates is strongly dependent on the sea-level curve, which has recently come under strong scrutiny (Pico et al., 2017; Dalton et al., 2019). In these situations an alternative approach is required to describe slip rates on faults, and how those slip rates evolve through time.

The Kaikōura Peninsula in the South Island of New Zealand (Fig. 1) provides an excellent example of this problem. The town of Kaikōura, which was strongly shaken and impacted by a tsunami during the 14 November 2016 Mw7.8 Kaikōura Earthquake (Clark et al., 2017; Goded et al., 2017; Hamling et al., 2017; Power et al., 2017; Stirling et al., 2017), is built around a flight of uplifted marine terraces (abrasion platforms) at the southern end of the Hikurangi subduction zone. Platforms such as these are cut at low angles (usually < 1° at Kaikōura; Inkpen et al., 2010) during sea level high stands, and the strandline that forms at their intersection with sea cliffs provides an extensive paleo-horizontal marker. Differential tilting of the Kaikōura peninsula has long been recognized (Ota et al., 1996; Campbell et al., 2005), but so far, only two single rates of uplift-at-a-point have been estimated, based on the age and elevation of the highest terrace (T1 - Fig. 2) at its highest point (1.1 mm/a. Ota et al., 1996), and on a flight of Holocene beaches (1.5 mm/a. McFadgen, 1987). These published uplift rates vary significantly and slip rate estimates have not been published for the underlying fault. The Mw7.8 earthquake of November 2016 provided independent documentation of coseismic landward tilting of the peninsula (Clark et al., 2017), along with several conflicting interpretations of faulting offshore of the peninsula (Clark et al., 2017;

E-mail address: Brendan.duffy@unimelb.edu.au.

https://doi.org/10.1016/j.tecto.2020.228460
Received 2 October 2019; Received in revised form 18 April 2020; Accepted 21 April 2020
Available online 13 May 2020

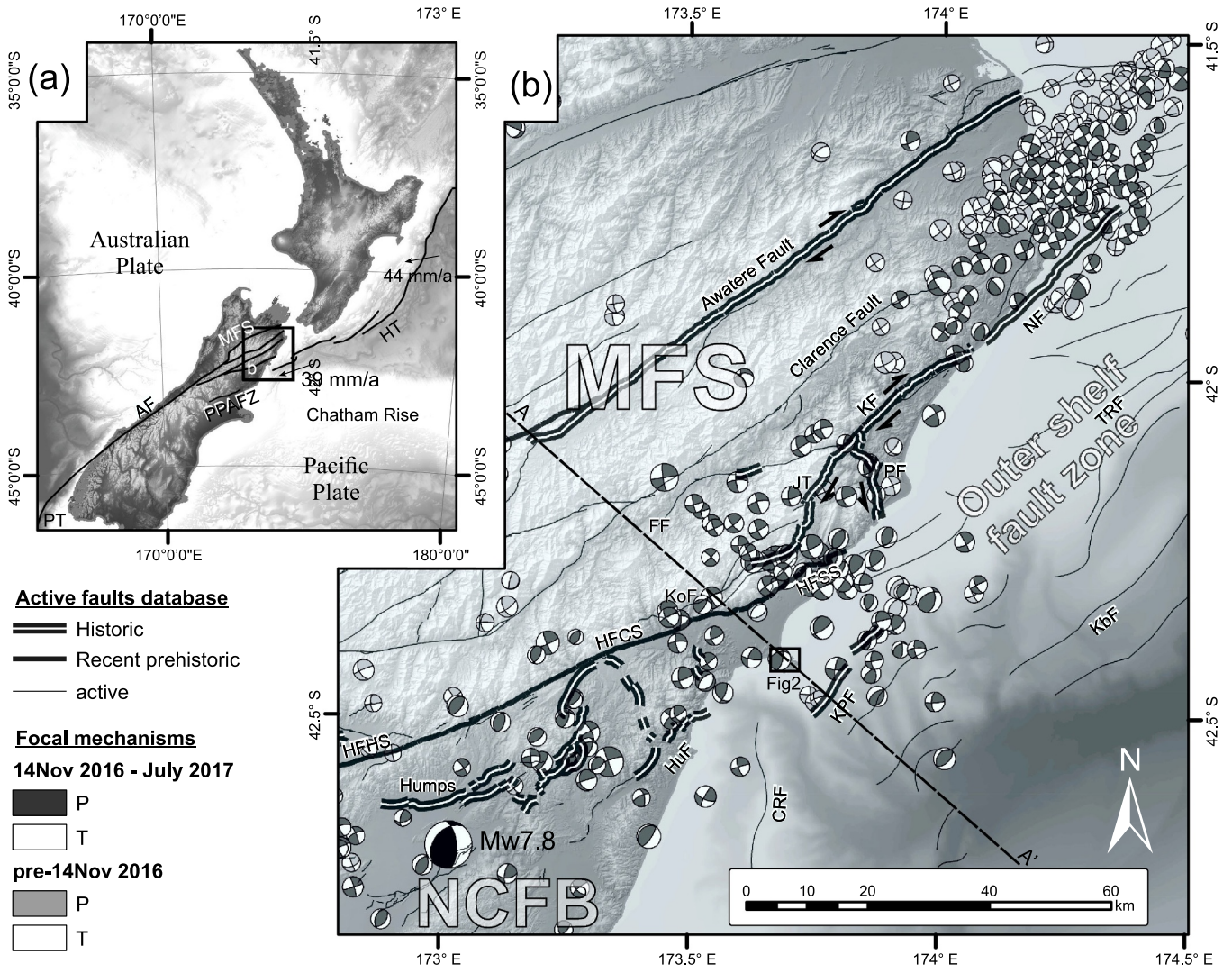

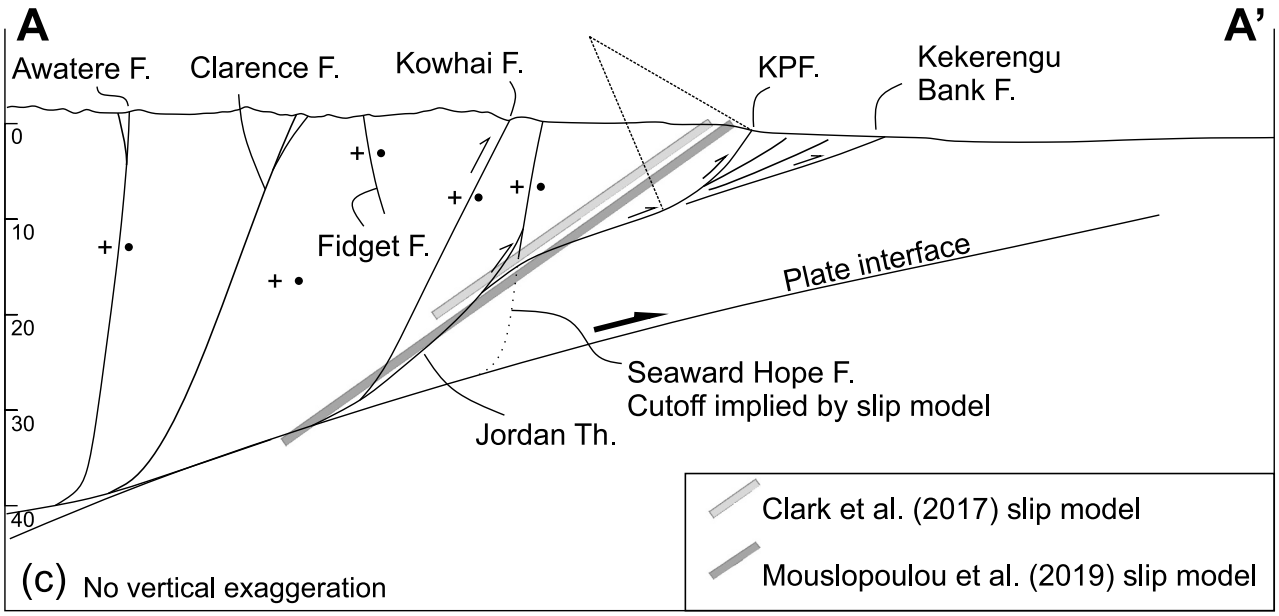

(caption on next page)

Fig. 1. A) New Zealand plate boundary setting and Demets et al. (2010) relative motion vectors (mm/yr) between the Australian and Pacific Plates. AF – Alpine Fault; MFS – Marlborough fault system. PT – Puysegur trench; HT – Hikurangi Trough; PPAFZ – Porters Pass Amberley Fault Zone. B) Shaded relief topographic and bathymetric DEM showing the location of the Kaikōura Peninsula (Fig. 2) relative to major offshore (Barnes and Audru, 1999; Walters et al., 2006) and onshore fault domains (Rattenbury et al., 2006; Litchfield et al., 2014), and historical surface ruptures including the Mw7.8 Kaikōura Earthquake (Stirling et al., 2017). It is not yet clear if the Kaikōura Peninsula Fault (KPF) ruptured to the surface but it is used in this study to calculate fault geometry and slip (see rationale in Section 5.1). Focal mechanisms show upper hemisphere plots of earthquakes from the Geonet catalog, downloaded 7 Aug 2017. Compressional quadrants are shaded. CRF – Conway Ridge Fault; FF – Fidget Fault; HFHS – Hope Fault Hurunui segment; HFCS – Hope Fault Conway Segment; HFSS – Hope Fault Seaward segment; Humps – The Humps Fault; HuF – Hundalee Fault; JT – Jordan Thrust; KBF – Kekerengu Bank Fault; KF – Kekerengu Fault; KoF – Kowhai Fault; KPF – Kaikōura Peninsula Fault; MFS – Marlborough Fault System; NCFB – North Canterbury Fold Belt; NF – Needles Fault; PKF – Point Kean Fault; TRF – Te Rapa Fault. C) Regional plate boundary cross section, showing the relationship of the Kaikōura Peninsula fault as defined here to major plate boundary elements and selected Kaikōura earthquake slip models for offshore thrusting below the Kaikōura Peninsula. Plate interface after Williams et al. (2013).

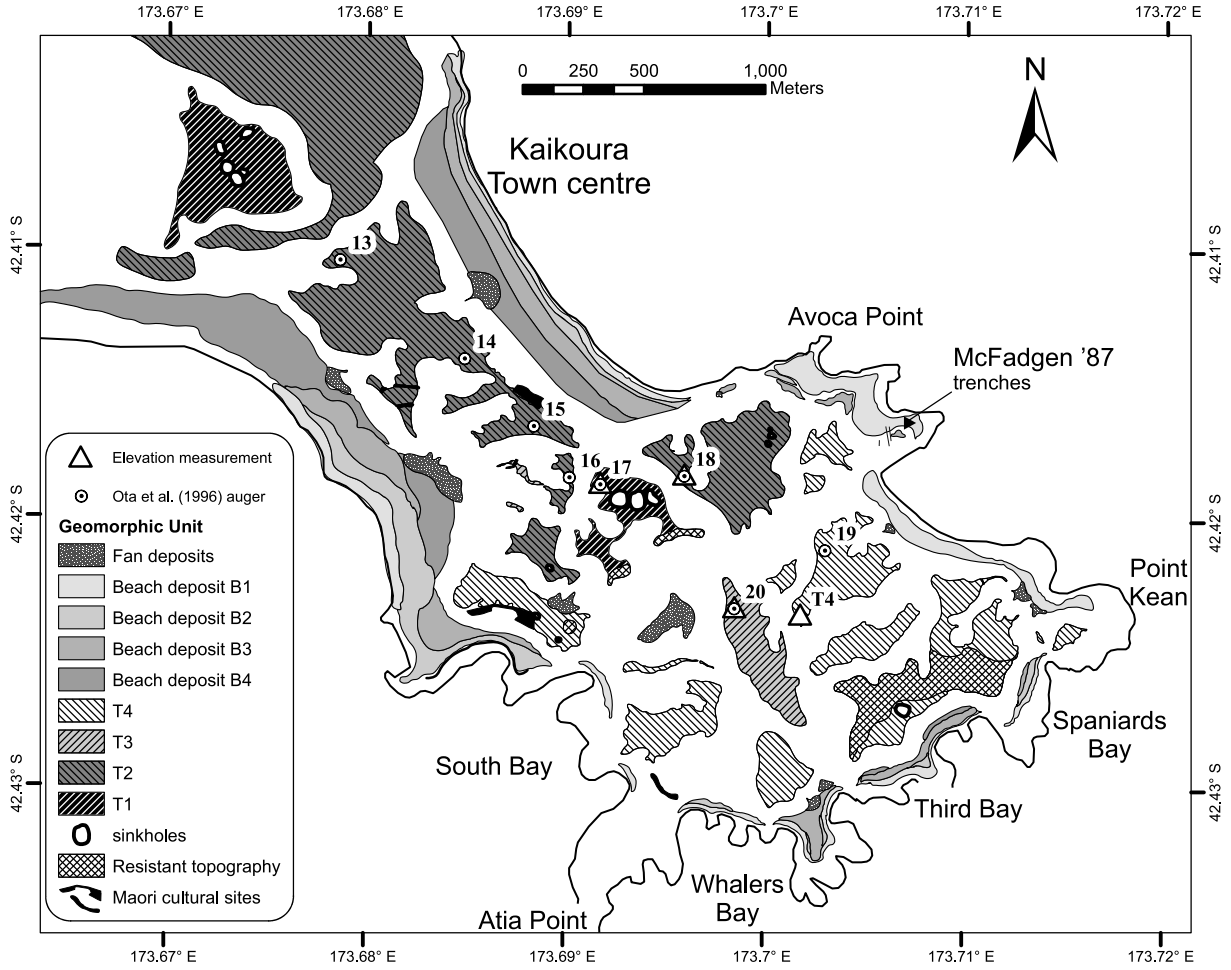

Fig. 2. Geomorphic map showing the extent and boundaries of the uplifted marine terraces at Kaikōura, and the locations of Ota et al. (1996) auger investigations. For location see Fig. 1.

Hollingsworth et al., 2017; Lanza et al., 2019; Mouslopoulou et al., 2019; Ulrich et al., 2019), so it is timely to evaluate how slip rates on the faults below the peninsula might have evolved over the late Pleistocene, and if/how modelled geometry and slip rate informs the debate about fault geometry and seismic hazard in this complex plate boundary transition zone.

This study employs a geometric approach to evaluate the rates of slip at 10^2-10^5 yr timescales on the thrust fault underlying the Kaikōura Peninsula. The geometry of the underlying thrust is estimated based on progressive tilting of terraces measured on a Lidar digital elevation model, using a variant of a method for fluvial terraces (Amos et al., 2007). The slip rate derived from terrace tilting is compared with rates derived from uplift of radiocarbon dated beaches (McFadgen, 1987), to facilitate discussion of the temporal variations in slip rates over Late Pleistocene to Late Holocene and historical timescales. Implications for the regional geometry of the Kaikōura Peninsula Fault and Late Pleistocene sea levels are also explored.

2. Study area

2.1. Regional neotectonic setting

The New Zealand plate boundary strikes NE-SW through the northern South Island of New Zealand, and transitions from westward subduction along the Hikurangi Trough to dextral oblique motion in the Marlborough Fault System (MFS) (Holt and Haines, 1995; Wallace et al., 2012) and the Alpine Fault (Norris and Cooper, 2001; Barth et al., 2012) (Fig. 1A). Subduction of the Pacific Plate declines southward along the Hikurangi margin toward the Kaikōura Peninsula, as the plate motion is progressively transferred to upper plate faults of the MFS

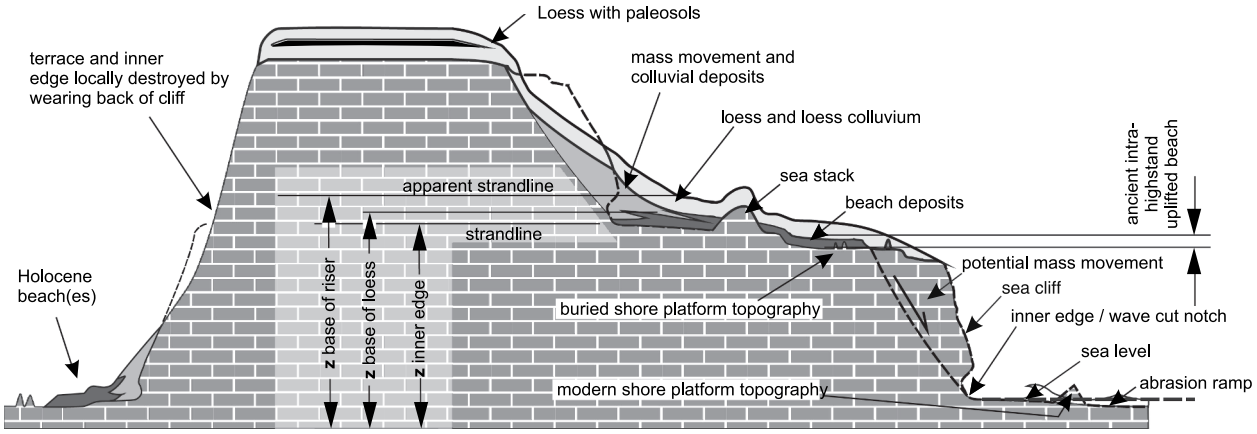

Fig. 3. Generic cross section through a flight of terraces like Kaikōura, showing the geomorphic and sedimentological factors that contribute to the terrace surface elevations. Note that cover sediments build up and out from the original location of the inner edge.

(Wallace et al., 2012). However, Clark et al. (2015) documented subsidence in the northeasternmost parts of the South Island (Fig. 1B), resulting from megathrust activity, indicating that the subduction thrust remains active offshore of the South Island.

The Hope Fault, located ~15 km northwest of Kaikōura (Fig. 1B), is the fastest slipping fault within the MFS. The Conway Segment of the Hope Fault accommodates about 23 mm/yr (Langridge et al., 2003) of a total of ~39 mm/yr of oblique convergence (DeMets et al., 2010). The remainder is distributed across the Kekerengu, Clarence, Awatere and Wairau Faults of the MFS (Knuepfer, 1992; Little and Jones, 1998; Langridge et al., 2010; Wallace et al., 2012). The slip at the eastern end of the Conway Segment transfers through a restraining left bend into the Jordan thrust that causes uplift of the Seaward Kaikōura mountains and links northward with the Kekerengu Fault (Van Dissen and Yeats, 1991; Little et al., 2018), although much of the slip in the recent earthquake was partitioned onto the Papatea Fault in the footwall of the Jordan Thrust (Hamling et al., 2017; Hollingsworth et al., 2017; Stirling et al., 2017; Litchfield et al., 2018; Diederichs et al., 2019).

The remaining slip is transferred offshore through the Seaward Segment of the Hope Fault and into the Outer Shelf Fault Zone close to the Hikurangi Margin (Barnes and Audru, 1999), a structural high that bounds the eastern edge of the continental shelf (Fig. 1). The seaward segment of the Hope Fault is strongly transpressional, marking an abrupt transition from the strike slip on the Conway segment (Pettinga et al., 2019), and the outer shelf fault zone includes NE-trending, dextral oblique thrust faults, as well as strike slip faults with orientations close to the plate motion vector. Seismic reflection surveys show that thrust faults such as the Te Rapa Fault dip at ~60° but display growth strata on the backlimbs of their fault-related anticlines, indicating that they could be listric at depth (Barnes and Audru, 1999).

Offshore of the Outer Shelf Fault Zone, the Kekerengu Bank Fault marks the limit of strong contraction. The fault has been active since the early to mid-Quaternary based on biostratigraphic ages of samples from the deepest synkinematic strata (Barnes et al., 1998). Its dip is not well-resolved beyond the first second of two-way-time but it has been interpreted as soling onto the subduction interface at depth (e.g., Fig. 12 in Barnes et al., 1998).

South of the Hope Fault, intraplate deformation is both slower and more complex than within the MFS and the offshore structure is poorly defined; however, the bathymetry deepens abruptly to > 800 m at the shelf edge, ~6 km east of the peninsula. This bathymetric escarpment was tentatively attributed to the Kaikōura Peninsula Fault (Duffy, 2014; Barrell, 2015).

The southernmost iteration of the MFS is probably the Porters Pass Amberley Fault Zone in North Canterbury (Fig. 1A). This fault zone has been evolving for only 0.8–0.4 Myr (Nicol et al., 1994) and has a much lower slip rate than the Hope Fault at only ~3–6 mm/yr (Cowan, 1992; Howard et al., 2005; Wallace et al., 2012). The Porters Pass Amberley Fault Zone is separated from the MFS by the North Canterbury fold and thrust belt (Yousif, 1987; Nicol et al., 1994; Litchfield et al., 2003; VanderLeest et al., 2017). The North Canterbury Fold and Thrust Belt is a zone of faults and folds with mixed orientations and kinematics, generally characterized by opposing vergences of predominantly west-dipping (e.g. the Hundalee Fault (Williams et al., 2018)) and east dipping structures such as the Kaikōura Earthquake progenitor Humps Fault zone (Nicol et al., 2018) and the offshore, east-dipping Conway Ridge Fault (Walters et al., 2006) (Fig. 1B). Cumulative slip rates in the North Canterbury fold and thrust belt are an order of magnitude smaller than in the MFS (Litchfield et al., 2014).

The offshore faults and the North Canterbury fold and thrust belt abut at the Kaikōura Canyon, ~5 km south of the uplifted marine terraces of the Kaikōura Peninsula (Fig. 1B). The shelf edge south of Kaikōura is completely dissected by the Canyon, which coincides approximately with an E-W boundary on the lower-plate between the oceanic Hikurangi Plateau to the north and the continental crust of the Chatham Rise to the south. The west-dipping fault systems north of the peninsula do not appear to extend south of the canyon and seem to be replaced by east-dipping faults like the Conway Ridge fault, suggesting that some complex transfer faulting occurs south of the peninsula (Nicol, 1991).

2.2. Kaikōura marine terraces

The Kaikōura Peninsula consists of a flight of uplifted Pleistocene marine terraces (Ota et al., 1996) (Fig. 2). The age, uplift and deformation of these terraces are described following the terminology defined by Pillans (1990). The terraces are old abrasion ramps developed on the various lithologies exposed in a train of well-exposed folds (Rattenbury et al., 2006). They appear as relatively flat surfaces that are correlated along the length of the peninsula; they are moderately well-preserved, commonly deeply dissected and draped in marine and non-marine cover sediments, which range in thickness from < 3 m on the lowest surface to > 6 m on the highest (Ota et al., 1996) (Fig. 4). The cover sediments typically consist of beach deposits and one or more loess blankets, and presumably colluvium derived from collapse of the ancient sea cliffs (Fig. 3). The present elevation of the marine terrace surfaces is the sum of the elevation of the wave-cut platform and the thickness of the cover sediments.

The original terraces were sub-horizontal (< < 1°) prior to tectonic deformation, and the modern shore platform and beach area provides an indication of the probable topographic complexity below the blanket of cover sediments (Fig. 3). In some areas, particularly within the

outcrop extent of the weak Waima Siltstone at Point Keen and Apia Point on the seaward end of the Peninsula, the wide modern abrasion ramp terminates shorewards at a well-developed inner edge. In contrast, resistant lithologies such as the Spyglass Formation commonly form jagged outcrops that protrude 1–3 m above the level of the abrasion ramp. Several sea stacks of Amuri Limestone dot the coastline on the eastern end of the peninsula (Fig. 3). Up to four levels of beaches, some with elevations > 7 m, separate the ocean and shore platform from the sea cliffs along much of the modern coastline.

Analogous features can be seen or inferred on the uplifted terraces. The uppermost terrace has a section along its seaward end that protrudes > 2 m above the terrace surface. This section is draped by loess and its character is unclear but it may be similar to the jagged outcrops that protrude above the modern abrasion ramp. Sea stacks are also found on several terrace levels (T2, T3) and small inset terraces analogous to the flight of minor beach surfaces can be seen on T3. In addition to these features, small excavations and embankments mark the presence of pre-European Maori fortifications around the edge of the first terrace level at strategic locations (Fig. 5d).

2.3. Kaikōura earthquake

The Kaikōura earthquake initiated on the south-dipping Humps Fault of the North Canterbury fold and thrust belt (Nicol et al., 2018) and ruptured northwards, progressively triggering elements of the MFS and North Canterbury fold and thrust belt. Surface rupture seems to have occurred on the Seaward Segment of the Hope Fault (minor), the Jordan Thrust, the Kekerengu Fault and the (Kekerengu extension) Needles Fault offshore, in addition to a number of smaller structures within the North Canterbury fold and thrust belt (e.g., Hamling et al., 2017; Litchfield et al., 2018; Nicol et al., 2018; Williams et al., 2018).

It was not initially clear whether low angle thrusts at the deformation front ruptured (Hollingsworth et al., 2017) or not (Hamling et al., 2017) but offshore thrusting of some sort, south of the Hope Fault, is supported on the grounds of geodetic, kinematic and seismological observations, including aftershock relocations and tsunami modelling (Clark et al., 2017; Hollingsworth et al., 2017; Power et al., 2017; Lanza et al., 2019; Mouslopoulou et al., 2019). Geological mapping (Rattenbury et al., 2006) indicates that the depth to Torlesse supergroup basement below the peninsula is only 400 m in the core of the anticline, suggesting that the hanging wall of thrust faults consists primarily of basement rocks.

The Kaikōura earthquake resulted in both coseismic (700 mm) and post-seismic (> 70 mm) uplift at the Kaikōura permanent GPS station (not located on the peninsula) (Stephenson et al., 2017) and 800–1000 mm on the peninsula (Clark et al., 2017).

3. Geomorphology of the Kaikōura peninsula

3.1. GIS analyses

This paper utilizes a subset of a 2012 Lidar survey of the Kaikōura region, acquired by the regional council (Environment Canterbury) and gridded at 1 m. This is the B4 dataset used by Clark et al. (2017) and metadata are provided in the supplement to their paper. The terraces were mapped in 3D using LeapfrogGeo software, as well as in ArcMap. The uppermost terrace has long been recognized to be tilted (Ota et al., 1996; Campbell et al., 2005), but inspection of the Lidar survey revealed a progressive tilting of terraces to the northwest (Figs. 4 & 5).

Terrace tilt was evaluated on orthographic projections of the terraces, by assuming that the terraces formed with an initial geometry that is similar to the present extensive wave-cut platform, and thus that the inner edge of the uplifted surfaces, presently buried below loess and colluvium, would have formed a horizontal strandline. These apparent strandlines are presently horizontally and vertically offset from the true strandlines because of the thickness of cover sediments (Fig. 3), but their maximum elevations are approximated by the abrupt changes in slope at the base of the degraded sea cliffs. This change in slope forms a line that is circuitous in map view but appears approximately straight when viewed horizontally and parallel to the strike of the surface. The true strandline should be approximately parallel to the apparent strandline, if there is no systematic down-dip change in cover sediment thickness. The tilt direction of the terraces was thus established by looking for section-view alignment of equivalent terraces on opposite sides of the peninsula; if the terrace is viewed oblique to tilt, a parallax effect will cause equivalent terraces to appear vertically displaced from each other. The best alignment of equivalent terraces across the peninsula occurs when the peninsula is viewed toward 226 ± 5°, parallel to the shelf edge and to some estimates of the modelled offshore thrust (Hollingsworth et al., 2017).

3.2. Late Pleistocene marine terraces

The tilting of the terraces (Fig. 4) is in keeping with recently documented coseismic tilting (Clark et al., 2017) but is not reflected in Ota et al.'s (1996) terrace correlations, which relied on limited loess and paleosol data (Fig. 4). In Ota et al. (1996), the western part of T3 projects into T2 and is poorly correlated with its inferred equivalent east of T1. Their T2 has 2 paleosols at localities 16 and 18, while their T3 is defined based on a single paleosol at locality 20. However, their auger localities 13 and 15, from their terraces III and II respectively, are virtually indistinguishable, and cannot be clearly tied to either T2 or T3 based on paleosol and loess stratigraphy. Ota et al. (1996) note that beach gravel at locality 20 is also present at localities 13 and 14; however, it is also present at 15, 16 and 18. Given the apparent deficiencies in Ota et al.'s (1996) previous correlation arguments based on loess stratigraphy, the auger logs are used here only for establishing cover thickness (Fig. 4).

Fig. 5 shows the revised correlations of the main terrace surfaces recognized here, each of which are present on both sides of the peninsula. These correlations form the basis of the geomorphic map presented in Fig. 2. Terrace T1 is present on the west of the state highway, and in the central parts of the peninsula. Terrace T2 fringes T1 on the north and south sides of the peninsula and forms the spine of the western part of the peninsula. Terrace T3 is mostly preserved as a ridge that runs parallel to the peninsula east of T1 and T2, although a minor remnant can be seen as a marked break in slope in the cliffs below the T2 surface, immediately south of the westernmost T1 terrace on the peninsula. This remnant provides an additional constraint on the dip of the T3 surface. Terrace T4 forms an extensive surface at the lower elevations of the peninsula, southeast of Avoca Point. Several minor terraces are evident, but they are subsidiary to the major terraces and have limited extents. These revised terrace correlations are as consistent with the thicknesses and stratigraphy of loess on each terrace as those proposed by Ota et al. (1996). The terraces are tilted at angles ranging from 0.71° (min – T4) to 1.12° (max - tilt of T1). A summary of measured terrace tilts is given in Table 2.

3.3. Holocene beach ridges

The elevations of the beaches that fringe the peninsula are problematic to define because; 1) they are culturally modified by cut-and-fill of building platforms, and 2) individual storm berms and associated beaches tend to increase in elevation in the middle of bays and decrease at the headlands, where most of the wave energy is expended on bedrock outcrops seaward of the beach. Profiles were measured along the crests of beach ridges and distributions fitted to the combined elevation datasets. Prominent beach ridges around Spaniards, Third and Whalers Bays at the eastern end of the peninsula (Fig. 2) have elevations, relative to pre-Kaikōura earthquake mean sea level, of 3.45 ± 0.5 m, 4.8 ± 0.5 m and 5.9 ± 0.5 m. Higher elevations are only associated with small debris fans. Two beach ridges along the northern side of the

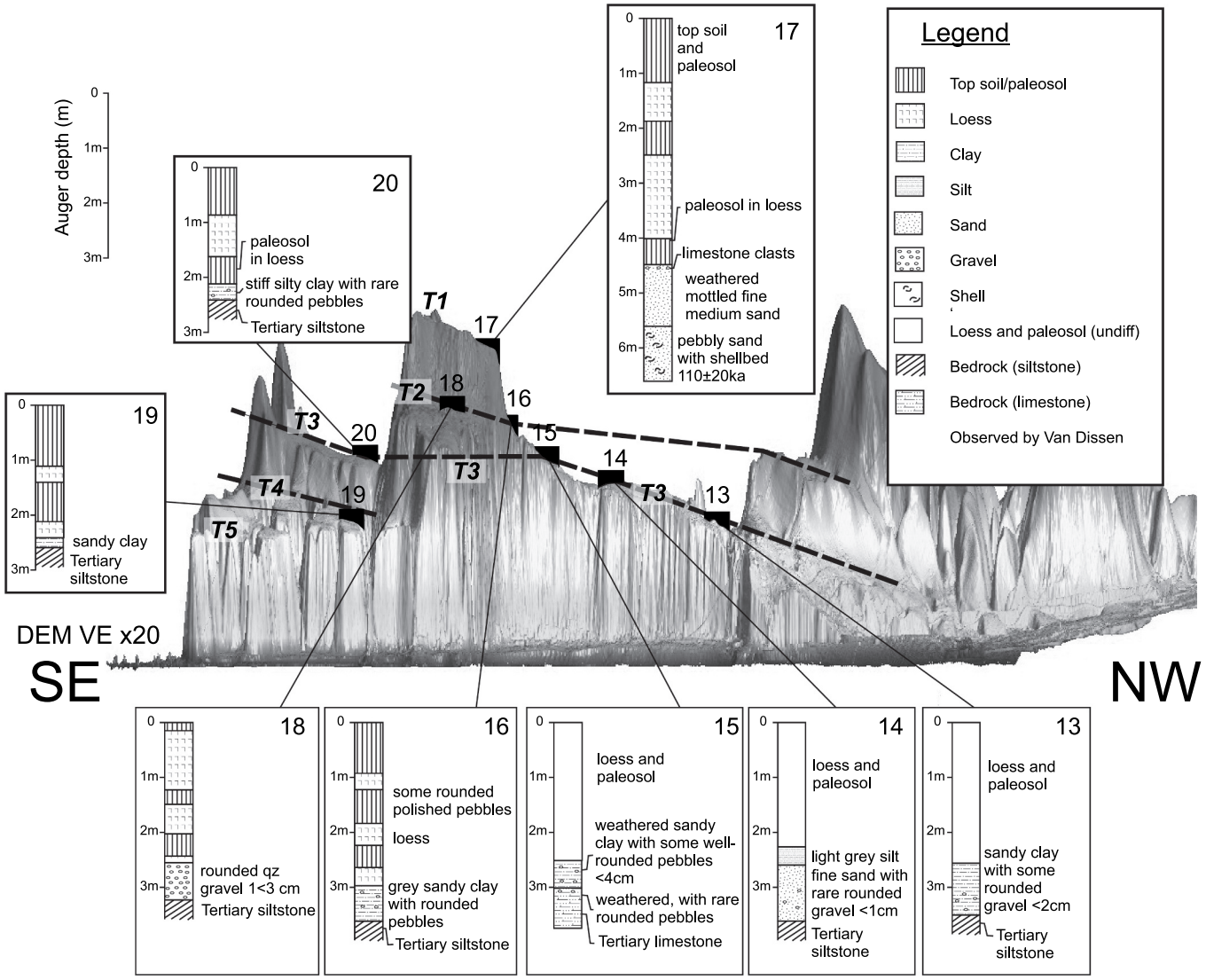

Fig. 4. View SW toward 226° of the Kaikōura lidar DEM, showing terrace correlations and cover stratigraphy from Ota et al. (1996) in the context of terrace tilt. Heavy dashed lines indicate the geometry implied by Ota et al.'s (1996) correlations. The cover sediment stratigraphy for their critical localities shown along the bottom of the image (T2/T3) is particularly ambiguous because the overall cover thickness does not vary significantly, and the loess interval lacks definition. Note that locality 13 was previously terrace T3 while 15 was previously terrace T2. On their T3, the cover thickness at locality 20 is substantially thinner than at 'equivalent' localities 13 and 14.

peninsula within the town limits have been significantly cut-and-filled. Within the limitations imposed by this modification, these seem to lie at 5.7 ± 0.6 m and 7 ± 0.5 m. The beach fronted by the modern storm berm is 3.12 ± 0.62 m, which overlaps substantially with the 3.45 ± 0.5 m beach on the eastern end of the peninsula. Beaches on the south side of the peninsula are also extensively modified but are at elevations consistent with those elsewhere on the peninsula. The highest is a small relic at 7 ± 0.5 m and relates to the same elevation beach on the north side. Slightly lower than this, a beach at 6.1 ± 0.5 m is interpreted as equivalent to the 5.7 ± 0.6 m on the north side. A third beach at 4.5 ± 0.5 m is the most extensive and is considered to be equivalent to the 4.8 ± 0.5 m beaches around the east end of the peninsula. The lowest beach on the south side has been modified by construction of a channel and artificial berm along much of the south coast but seems generally consistent with the modern 3.45 ± 0.5 m beach elsewhere. Based on the beaches measured across 28 lidar profiles, the elevations of beaches surrounding the Kaikōura peninsula are therefore given as 7 ± 0.5 m; 5.8 ± 0.7 m; 4.6 ± 0.6 m and 3.45 ± 0.5 m. These elevation ranges incorporate the variability arising from different wave climates in different parts of the peninsula and from any long wavelength tilting.

The beach ridges mapped from lidar can be related to those surveyed by McFadgen (1987), who excavated two trenches across beach ridges on the peninsula (see location on Fig. 2). Rather than using an absolute datum, McFadgen's (1987) logs report elevations above the crest of the growing beach ridge. Three beach ridges higher than the pre-quake modern ridge are present, with elevations of +1.1 m (McFadgen B, equivalent to the 4.6 ± 0.6 m beach 2), +1.9 to 2.1 m (McFadgen C, D, equivalent to the 5.8 ± 0.7 m beach 3) and + 3.2 m (McFadgen E, equivalent to the 7 ± 0.5 m beach 4). McFadgen interpreted that beaches C and D were both deposited between the same two events.

4. Marine terrace tilting and fault geometry

In situations where terraces are deformed above thrust faults, it is common practice to use geometric models of fold and thrust evolution to unravel the cumulative deformation history of the surfaces (Amos et al., 2007; Le Béon et al., 2014). Each model predicts different patterns of surface uplift (Fig. 6), so application of these models requires

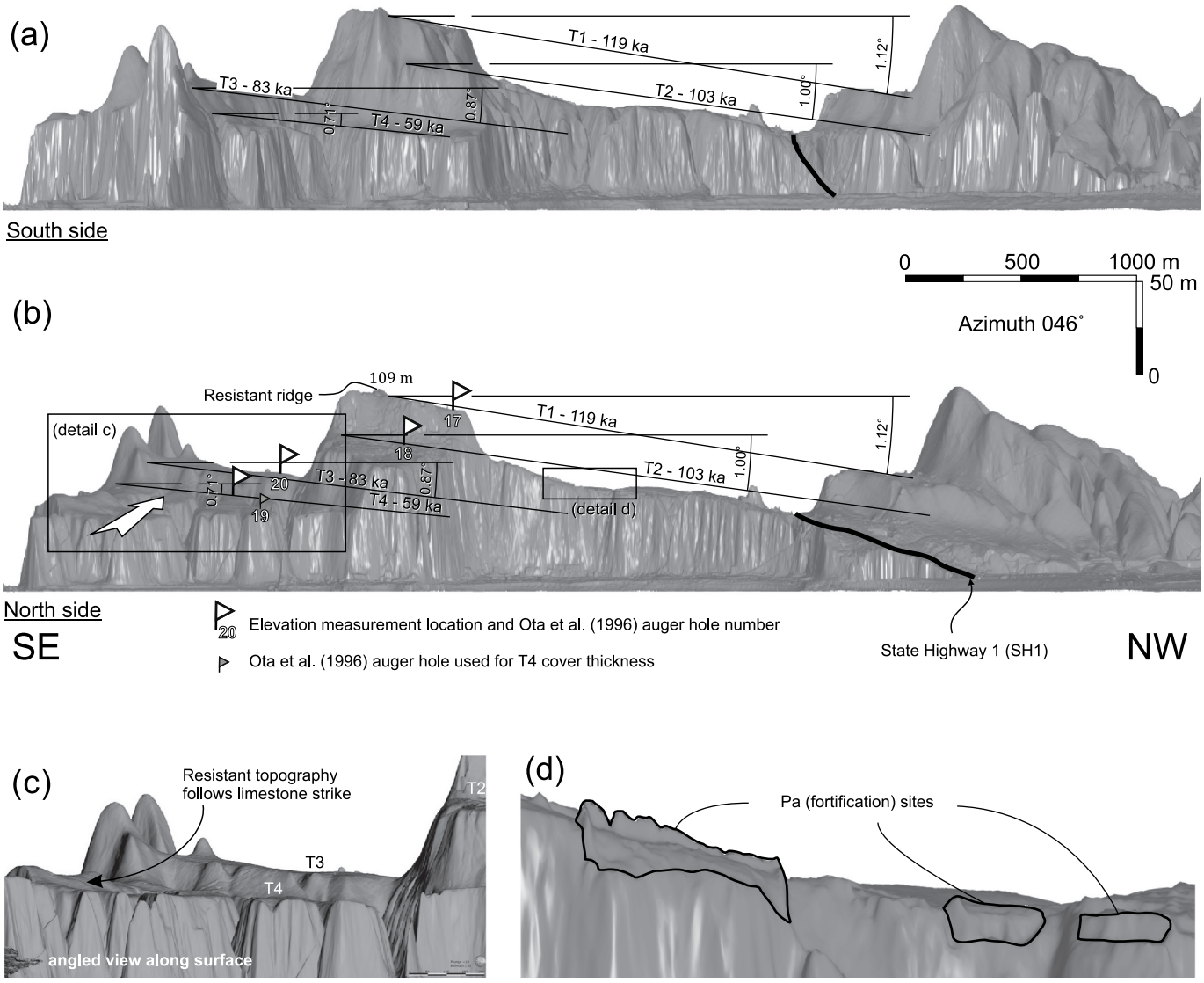

Fig. 5. 8× vertically exaggerated LiDAR DEM of the Kaikōura Peninsula, showing tilted surfaces viewed from both southwest (a) and northeast (b), and revision of Ota et al.'s (1996) terrace correlations. Solid lines show the terraces rotated from paleo-sea level based on the model. (c) View along surface of T4 in direction of white arrow on (b), showing the apparent bulge in T4 caused by the buried outcrop of the Spyglass Formation limestones (see resistant topography on Fig. 2).

observed patterns of differential uplift, recorded by terrace geomorphology, to be compared with patterns predicted by kinematic models.

The geometry of the backlimb is particularly diagnostic of the faulting model. End member models for fault-bend folding, fault-propagation folding and trishear fault-propagation folding produce a pattern of differential terrace uplift that reflects the dip of planar fault segments (Fig. 6A–C). If an uplift is driven by these styles of folding, a planar surface that is cut on the foreland side of the fault bend syncline will be carried passively up the ramp, while the platform cut on the hinterland side will bend into parallelism with the ramp. Uplift is uniform except where the terrace surfaces pass through the active syncline and up the ramp. There, consecutive surfaces will have different limb lengths, but equal limb dips. Differential uplift is generally uniform within dip domains (Hardy and Poblet, 1994) and progressive limb rotation in fault propagation folding is confined to the forelimb of the fold. These models are inconsistent with the observational data and are therefore discarded.

Three main models provide an explanation for progressive backlimb rotation of successively developed, paleo-horizontal geomorphic markers. Shear fault bend folding (Fig. 6D) results in tilting of terraces due to limb rotation as a weak layer at depth undergoes simple shear at a fault-bend (Suppe et al., 2004). The presence of a discrete fault bend requires that the fold growth includes a component of limb lengthening by kink-band migration up the ramp. This results in terraces that display a combination of progressive backlimb tilting caused by simple shear, and a domain of constant tilt caused by particle migration through an active axial surface.

Detachment folds develop when a competent horizon detaches from a weaker horizon along which a fault is propagating at depth (Fig. 6E). The fold amplitude grows by gradually tightening, resulting in limb rotation as the slip accumulates on underlying fault (Hardy and Poblet, 1994). A sequence of terraces eroded into a detachment fold will display an increase of tilt with age (e.g., Rockwell et al., 1988). The limb length remains constant but as the limbs steepen, the fold crest widens, and the deforming surfaces are kinked between the axial surfaces outside the box fold. The net result consists of a zone of rotation on either limb of the fold, separated by a zone of relatively uniform uplift.

Folding of a terrace surface above a listric thrust fault (Fig. 6F) produces a distinctive pattern of non-uniform rock uplift rates, associated with smooth progressive rotation of the backlimb with accumulating slip as the terrace passes through the axial surface separating the planar and listric parts of the fault (Seeber and Sorlien, 2000; Amos

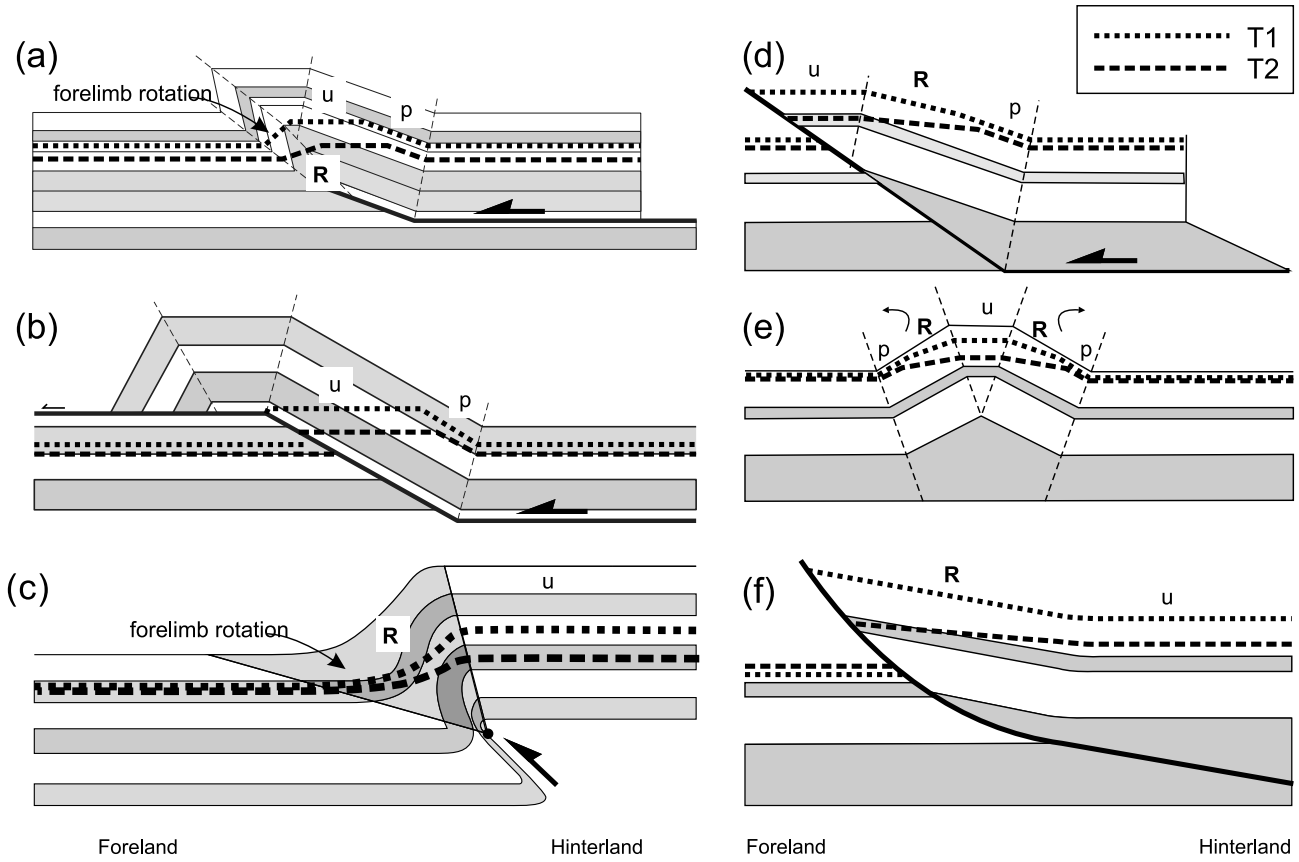

Fig. 6. Terrace deformation superimposed on simple kinematic models for fault-related folding. Annotations: u – Uniform uplift; p –ramp-parallel; R – rotation. A-C do not produce a progressive rotation of the backlimb, whereas D-F do so. Fault propagation folding (A) (Suppe and Medwedeff, 1990), results in rotation of the terrace only on the forelimb of the fold, with uniform uplift across the crest and rotation of the terrace to parallelism with the ramp on the backlimb. A fault-bend fold (B) (Suppe, 1983) produces the same pattern of backlimb deformation, whereas trishear folding (C) (Erslev, 1991) results in rotation of the forelimb, and relatively uniform and horizontal uplift of terraces above the fault. Simple shear fault bend folding (D) (Suppe et al., 2004) results from shear of an incompetent layer at depth, and causes progressive rotation of only part of the terrace segment. The down-dip terrace treads become parallel to each other where they have passed through the synclinal axial surface together. A similar pattern forms on both limbs of a detachment fold (E (Hardy and Poblet, 1994)). A listric fault (Seeber and Sorlien, 2000; Amos et al., 2007) results in smooth, progressive rotation of the backlimb as the terrace passes through the axial surface separating the planar and listric parts of the fault.

et al., 2007). In cases where the listric section merges with a planar ramp at depth, the deformed terraces will transition from progressive tilting above the increasing fault dip of the listric fault plane, to uniform uplift above the planar ramp. This pattern of differential uplift is similar to patterns of limb rotation and terrace tilting that could develop over a multibend fault bend fold (Medwedeff and Suppe, 1997) or by kink band migration across a discrete bend in a thrust fault ramp (Le Béon et al., 2014). However, these examples can be approximated by listric faulting (Seeber and Sorlien, 2000).

In general, the terraces at Kaikōura fan consistently, with progressive rotation of the surfaces and no parallelism of older and younger terraces. These characteristics are inconsistent with the models in Fig. 6A to E. The smooth rotation implied by the progressive fanning shown in Fig. 5 is consistent with backlimb deformation caused by listric faulting at depth. Any transition to a planar ramp must lie landward of the peninsula because the tilt of the terraces is continuous within the coverage of the lidar survey. This paper therefore adopts a listric fault model for the deformation of the Kaikōura terraces.

5. Fault geometry producing uplift of Kaikōura peninsula

5.1. Point Kean Fault

The Point Kean Fault (Fig. 1b) has become embedded in the literature as an important part of the 2016 Kaikōura earthquake rupture and the fault responsible for deformation of the Kaikōura Peninsula, but its geometry seems to become increasingly controversial. Stirling et al. (2017) report that the Point Kean fault rupture was down to the NW, and probably strike slip (c.f. Litchfield et al., 2018 who report that no horizontal displacement has been observed). Strike slip displacement would imply a steep dip, but Clark et al. (2017) assigned a low (35°) northwest dip to the Point Kean Fault (contrary to the observed sense of displacement) and used it to match the observed tsunami record and uplift of the Kaikōura Peninsula. Clark et al. (2017) project their putative fault southwest along strike to pass approximately halfway between Point Kean and the shelf-edge. Litchfield et al. (2018) follow Clark et al.'s strike but adopt a steeper dip of 55 ± 15°. Stirling et al. (2017) cite Barrell (2015) to suggest that the Point Kean Fault is required to match prehistoric shore platform uplift, though Barrell did not invoke a fault in that location.

Aftershock relocation might be expected to resolve the issue of fault geometry but has proven problematic and relocations of the same dataset are difficult to reconcile (compare Lanza et al., 2019; Mouslopoulou et al., 2019). Nevertheless, relocated aftershocks suggest that the Point Kean fault is either more steeply dipping than the 55° inferred by Litchfield et al. (2018) (Lanza et al., 2019), or part of an 'offshore splay thrust fault' that reaches the surface along the shelf edge (Mouslopoulou et al., 2019), or both. The offshore splay coincides with the location of an offshore fault inferred by Barrell (2015) and referred to here as the Kaikōura Peninsula Fault (Fig. 1b). These are critical

distinctions given the importance of the 'Point Kean fault' as the link between the southern and northern components of the entire Kaikōura Earthquake ruputure cascade; Ulrich et al. (2019) found that the observed GPS displacements require a greater dip-slip component, and thus more northerly strike, on the Point Kean fault compared with the geometry proposed by Clark et al. (2017); ultimately, most recent work is more consistent with a shelf-edge fault than the originally inferred, shallow NW-dipping geometry of the Point Kean Fault. The outcropping Point Kean Fault is probably a small strike slip fault or a backthrust in the hanging wall of the Kaikōura Peninsula Fault.

5.2. Structural model for the Kaikōura Peninsula Fault

The 3D alignment of equivalent terraces on the north and south sides of the peninsula suggests that they strike 226°, which aligns with the shelf edge fault previously proposed by Barrell (2015) and (Duffy, 2014). Below, I explore several options for dip and location, ranging from 60° based on the dip of the Te Rapa shelf-edge listric thrust fault (Barnes and Audru, 1999), to 30° dipping structures both further offshore (e.g., the Kekerengu Bank Fault) and closer inshore, e.g., the putative Point Kean Fault (Clark et al., 2017). I assume dip-slip only. Major assumptions are dealt with in Section 5.2.2.

5.2.1. Fault curvature and slip calculations

A geometric solution was calculated relating the tilt of the terrace to the slip on the [listric] Kaikōura Peninsula Fault, and on a range of other possible structures. Fault curvature and slip were calculated for each surface following a procedure modified from Amos et al. (2007), illustrated in Fig. 7 and detailed in the electronic supplement to this article. The calculations involve determining the radius of curvature of a putative fault, and its slip, from the tilt and vertical separation of the marine terraces.

5.2.2. Model assumptions

Even though listric geometry is consistent with the observational data of both the earthquake and the uplifted terraces, several assumptions contribute sources of error and uncertainty to the analysis. A detailed description of the uncertainties is provided in Table 1. The magnitude of these uncertainties was estimated within reasonable bounds and accounted for in a 10,000-iteration Monte Carlo simulation in the @RISK 6 Excel add-in. All error bars quoted in this paper are at the 95% confidence level, unless otherwise indicated.

5.2.3. Terrace elevation-at-a-point

The technique illustrated in Fig. 7 relies on a robust measurement of elevation at a point (Z_X on Fig. 7) that is located a known distance from the fault. Z_X was measured by using a combination of lidar and the Ota et al. auger hole logs. The highest terrace (T1) is located in the center of the peninsula, and reaches a maximum elevation of 109 m (Fig. 5b). The terrace is approximately flat and no inner edge can be defined except at the northwesternmost end of the terrace tread. The maximum elevation occurs along a linear ridge that marks the eastern end of the terrace and coincides with the mapped extent of the resistant Spyglass Formation limestone. This ridge is approximately 1.0–2.4 m high, which is similar to the protrusion of outcrop of the Spyglass Formation limestone above the modern abrasion ramp, relative to softer Amuri

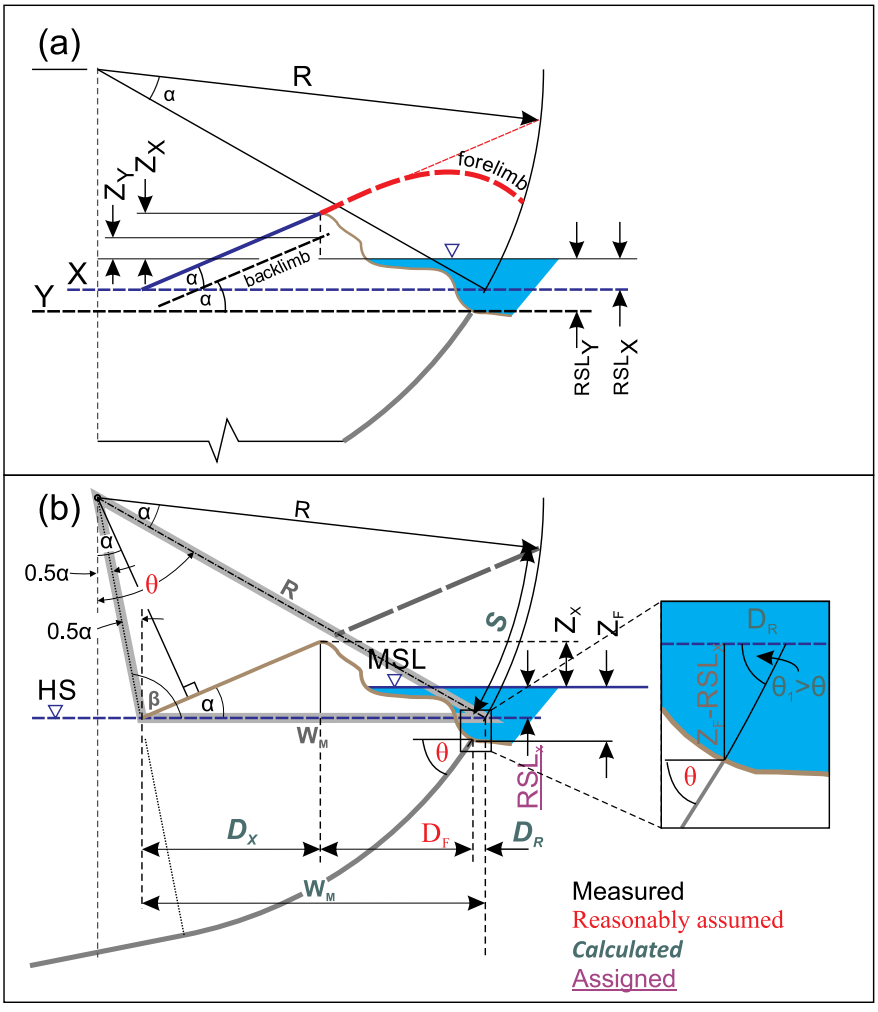

Fig. 7. A) Illustration of the geometry of tilted terraces. For a given rotation = α, an equivalent age terrace X that started at RSL has an elevation Z; terrace Y, which started deeper at RSL has a lower elevation Z . B) Parameters used to calculate the X X Y Y radius of curvature and slip on the fault, given its tilt and elevation. Calculations are based around the geometry of the heavy grey triangle. α – angle of tilt of terrace; θ – fault dip at seabed; θ – fault dip at paleo-sea level; D – distance from submarine fault 1 F trace to elevation measurement location; D – distance from submarine fault trace to fault-RSL projection = (Z − RSL)/tanθ; MSL R F 1 – mean sea level; R – Radius of curvature; RSL – relative sea level at time of cutting of surface X; Z –elevation of surface X above X X MSL at measurement location; Z – depth of fault submarine trace below RSL = Depth - RSL;W – horizontal distance between F X X M fault/RSL intersection and terrace/RSL intersection. Details of calculations are contained in the online supplement to this article. It is not feasible in this instance to calculate the dip of the planar ramp (c.f., Amos et al., 2007).

Table 1
Uncertainties and assumptions associated with application of the listric fault analysis to Kaikōura in this study.

Assumption/uncertainty	Description	Managing uncertainty
Assumptions regarding the location (Df), depth to trace (Zf) and dip (θ)	A priori, a range of options are feasible in terms of fault location (shelf edge to Kekerengu Bank) and fault dip (< 30 to 60°). Combined with the 250 m spatial resolution of the bathymetry data, this creates possible errors in determination of the location and depth of the fault trace.	Uncertainty regarding location is accounted for by investigating several scenarios for both locations and fault dip. For each scenario, measurement errors associated with the bathymetry data are estimated to be: Df ± 1000 m; Zf ± 100 m
Assumption that all terraces reflect major sea-level high-stands	This analysis implies that each terrace represents a prolonged high-stand and that minor fluctuations or individual uplift events are a minor part of any long-term record.	The assignation of the terrace levels to prolonged high stands is supported by the fact that the surfaces are developed by bedrock erosion. Shore platforms have eroded at rates of 0.525 to 1.181 mm. a − 1 for the last four decades (Stephenson et al., 2019). Individual uplift events will not be recorded during low-stands, as they will be re-abraded following uplift. Some/many individual uplift episodes during high stands may not be preserved as marine terraces, as they are eventually removed by wearing back of the cliff (Stephenson et al., 2017) or buried by cliff collapse following sea-level fall. However, sea level high stands should overall abrade wide shore platforms.
Uncertainty regarding choice of relative sea-level curve (RSL)	Pillans (1990) pointed out uncertainties in the dating of the Papuan global reference sea level curve, particularly the difficulties at that time of reconciling the Papuan curve with the oxygen isotope record. He cautioned against unrealistically detailed correlations, and suggested that the curve is not valid for use at uplift rates > 3 mm/yr. It is now well-understood that large scale variations occur in 'global' sea level resulting from glacio-isostatic effects	A substantially updated Papuan curve was initially used for this study (Duffy, 2017). However, difficulties remain when applying 'global' curves (Caputo, 2007) so this paper explores a regionally-derived curve based on New Zealand and southern Australia.
Uncertainty arising from variability of sea level during a single high stand (RSL)	Variations in sea level during a single highstand may exaggerate apparent uplift rates of some (young) features. For example, equatorial ocean syphoning (Mitrovica and Peltier, 1991) draws water from low latitudes toward a collapsing peripheral bulge, which serves to create a eustatic sea level fall following deglacial sea-level rise, such as over the last 4 kyr. Local effects may arise due to relative glacial loading of the South Island, versus the North Island.	The problem is not significant for terraces T1 through T4, but could be significant for beaches. We use Hayward's sea-level curve for New Zealand, which covers the appropriate Late Holocene timescale at the appropriate resolution.
Uncertainty arising from assignment of terrace ages	Only the uppermost terrace is dated; its age constraints are relatively poor and include three highstand scenarios. Undated lower terraces must be assigned ages by correlation with a sea-level curve, based on elevation and tilt relative to estimated RSL. Assuming rotation above a single fault (or average fault), feasible correlations for each terrace must 1) yield a similar independently calculated radius of curvature to the reference terrace, and 2) be geometrically feasible, i.e. yield a calculated Zx that is within RSL error of the actual Zx	The (weakly) dated top terrace is assigned to the last interglacial, and age and elevation of that and subsequent terraces are assigned based on the regional sea-level curve compiled for this study, and on the assumption (see above) that all terraces reflect major sea-level high-stands.
Uncertainty in the measurement of terrace tilt (α)	The exact location of the strandline at any point may be misidentified due to burial by cover sediments and colluvium. Strandline dip value is strongly dependent on the direction in which it is viewed. The highest terrace does not have a strandline that is extensive down dip and thus is susceptible to misinterpretation of its dip.	Dips were measured on a moderately vertically exaggerated section view of the lidar to optimize identification of the dip. The tilt of the apparent strandline was identified as the zone of maximum curvature along the down-dip extent of the terrace, as picked on a slope map draped over the 3D model. The preferred azimuth was selected by looking for vertical coincidence of equivalent terraces either side of the peninsula. Measurements were then obtained over a range of azimuths 5° either side of the preferred azimuth. The dip was estimated from the mean of the full range of measurements, and the uncertainty was estimated from its standard deviation. Uncertainties ranged around 10%.
Uncertainty arising from variability in the surface elevation at a point (Zx) of the measured surface, and variable cover bed thickness.	The surface elevation at a point x (Zx), is measured from the LiDAR and thus has little inherent error. However, the surface is buried by up to several meters of marine and loess cover sediments. The thicknesses appear to be relatively uniform for a given terrace (see also McFadgen, 1987), but modern shore platforms have as much as 2 m of relief (Amuri and Waima outcrop) and up to 4 m of relief (outcrop of resistant Spyglass Formation), which will persist below the cover sediments.	No measurements were taken in outcrop zone of Spyglass Formation. The cover sediment thickness is accounted for by subtracting Ota et al.'s (1996) cover thickness for the relevant terrace from its surface elevation. Relief on the buried surface is accounted for with a ± 1 m normally distributed uncertainty.

and Waima Formations. However, at many localities along the present coast, such as at the Point Kean seal colony, these elevated limestone outcrops occur < 100 m offshore of the modern sea cliff. The modern shore platform has an average seaward slope of 0.66 ± 0.4°, or a gradient of 1% (Inkpen et al., 2010). I adopt the north western part of the peninsular section of terrace T1 (Ota et al., 1996 locality 17, Fig. 5) for the elevation of the wave cut notch. The modern terrace surface there is at 95.9 m a.s.l and the abrasion platform is buried below at least 6.6 m of sedimentary cover, giving a maximum elevation of 89.3 ± 1 m (1σ). If this location was well seaward on the abrasion ramp, the true elevation could have been ~1 m higher. Bedrock was also not encountered in the hole, so the surface could be up to 1 m

deeper.

Terrace T2 reaches a maximum elevation of ~84 m. The inner edge is poorly defined on the north side because of the presence of building platforms and is buried by alluvial fans on the south side of the peninsula. West of terrace T1, the surface of T2 is the highest terrace on the peninsula and is markedly degraded by fluvial incision. The surface is undulating and varies between 3 m and 9 m lower than the projection of T2 above it. The outer edge of this part of the terrace is modified by Maori fortifications at several locations (Fig. 5). The terrace is present west of SH1 but the inner edge there is blurred by colluvial deposits. The elevation of the terrace is measured at auger locality 18 (Fig. 5b), where it has an elevation of 78.2 m, including 3.2 m of marine and non-marine cover sediments, giving a maximum elevation of 75 ± 1 m (1σ).

Auger locality 20 (Fig. 5b) is located on T3, just east of T1, and at an elevation of 63.2 m. It has a cover thickness of 2.4 m, giving an abrasion surface elevation of 60.8 ± 1 m (1σ).

Terrace T4 is the lowest terrace and is only present on the eastern end of the peninsula, where it is very extensive. Ota et al. (1996) mapped a lower terrace (their T5), but a view parallel to the supposed surface (Fig. 5) simply shows T4 and some topography consistent with the strike of resistant bedrock units at the eastern end of the peninsula. There is no well-developed T4–5 riser such as separates the other terraces. The inner edge of T4 is best estimated on the northern edge of T3 where its surface elevation is 50.7 m (Fig. 5b). A nearby auger hole (19, grey flag on Fig. 5b) has a reported cover thickness of ~2.6 m, giving an estimated elevation of the inner edge of 48.1 ± 1 m (1σ).

5.3. Selection of relative sea levels

The age of terraces is critical for estimating the RSL during abrasion. Moreover, sea levels cannot be reliably correlated with global sea level curves if the reference sites do not share glacio-isostatic characteristics (Pillans, 1990). Large-scale responses to ice-sheet dynamics, including glacio-isostatic adjustment and equatorial ocean syphoning (Mitrovica and Peltier, 1991), redistribute bathymetry and hence ocean water, challenging the application of global curves to regional neotectonic problems (Caputo, 2007). Although the Papuan sea level curve has been widely applied to New Zealand marine terraces (Bull and Cooper, 1986; Pillans, 1990; Berryman, 1993; Oakley et al., 2018), and has been repeatedly revised, improved and fit better with oxygen isotope records (Lambeck and Chappell, 2001; Woodroffe and Horton, 2005; Dutton and Lambeck, 2012), it remains difficult to reconcile with sea level data from closer sites such as South Australia. This paper therefore explores locally-derived relative sea-levels for the four major high-stands since and including the last interglacial. Many of the records are from South Australia, which is tectonically stable and lies at a comparable latitude with respect to large scale lithospheric responses to ice sheet dynamics.

The best age control on a Kaikōura marine terrace is presently provided by the extent of amino acid racemisation in fossil proteins of *Tawera spissa* molluscs within the marine cover sediments of T1, which Ota et al. (1996) used to calculate an age by calibration with a dated terrace at Wanganui in the North Island of New Zealand. Their age for the T1 terrace (110 ± 20 ka) has large uncertainties that represent both analytical uncertainties and an allowance for temperature differences between terrace T1 and the calibration sites; the result is an age that encompasses MIS 5c and 5e. Ota et al. (1996) argued that the relatively cool water fauna deposited on T1 is indicative that it formed during the cooler MIS 5c, rather than the warmer MIS 5e.

Based on faunal similarities, Ota et al. (1996) also correlated the Tarapuhi terrace at Haumuri Bluffs with MIS 5c, implying that T1 and the Tarapuhi terrace are equivalent in age. Oakley et al. (2017) obtained an infra-red stimulated luminescence age of 95 ± 10 ka for the highest Tarapuhi terrace at Haumuri Bluffs, south of Kaikōura, but later correlated the terrace with the first MIS 5c high stand and assigned it an age of 106.9 ka, outside their error range (Oakley et al., 2018). This apparent paper to paper discrepancy illustrates the difficulty assigning terrace ages in this region. Part of that difficulty may be attributable to Ota et al.'s cool temperature argument. In the modern Kaikōura environment, the balance between long-shore advection, upwelling and probably radiative forcing play a crucial role in determining coastal water temperatures and their variability with depth (Chiswell and Schiel, 2001). The dynamics of this system are likely to have been substantially different at a time when the coastal geomorphology was substantially different. Prolonged, wind-shear driven upwelling has been shown to cause extensive surface cooling in other New Zealand coastal environments (Longdill et al., 2008) and this possibility cannot be ignored here for a time when the peninsula was not emergent. Furthermore, tectonic complexities often result in varying earthquake histories and uplift rates, even over relatively short distances (Litchfield et al., 2020). Given the tectonic complexity between the Kaikōura and Haumuri Bluffs localities (Nicol, 1991), it is perhaps unwise to compare them too closely.

5.3.1. MIS 5e

MIS 5e is commonly assigned an RSL of +6 m but is very variable globally. In terms of levels, Hearty et al. (2007) show that sea level in Barbados rose from a stable 5e position at +2.5 m between 132 and 125 ka to a brief high of +9 m at 119 ka, at which age sea level fell to the 5d glacial sea level. This brief high is not recorded in stable continental Western Australia, although the timing of the fall and the magnitude of the highstand are broadly consistent at ~119 ka and +3 m respectively (Stirling et al., 1998). Murray-Wallace (2002) and Murray-Wallace et al. (2016) report MIS 5e sea level indicators preserved at +2.1 ± 0.5 m along stable cratonic coastlines in South Australia. These Australian levels are probably representative for the South Island because, a) the Canterbury and South Australian regions lie within 5° of latitude and thus in a broadly similar field relative to the Antarctic ice cap peripheral bulge; and b) Australia and New Zealand display similar magnitudes of mid-Holocene high stands and subsequent sea level falls, even despite local glacio-isostatic adjustment for Alpine glaciers (Sloss et al., 2007; Clement et al., 2016). An MIS 5e terrace in the southwestern part of the South Island New Zealand yielded an OSL age of 123 ± 7.0 ka (Cooper and Kostro, 2006), which agrees with the better-constrained age of sea level fall in Australia. Taking into account the possibility that the terrace was abandoned early in MIS 5e, I adopt an age and elevation for MIS5e of $119_{-2.5}^{+13}$ ka and +2.1 ± 1 m respectively, following the South Australian sites.

5.3.2. MIS 5a and 5c

Hails et al. (1984) reported RSLs of at least −8 m (MIS 5c, c.105 ka Lowly Point Fm) and −14 m (MIS 5a, c82 ka False Bay Fm) in South Australia's Spencer Gulf. In New Zealand, Shulmeister et al. (1999) reported sea levels at Banks Peninsula south of Kaikōura of −12.6 ± 2 m during MIS 5c and −15.4 ± 2 m during MIS 5a, although their ages lack precision. More recent records from Port McDonnell in South Eastern Australia provide an RSL at MIS 5c of c.-14 m (Blakemore et al., 2014). The timing there is poorly constrained. However, Cutler et al. (2003) found that MIS 5b sea level was −58 m at 92.6 ± 0.5 kyr, having dropped about 44 m in approximately 10 kyr during the MIS 5c to 5b transition. This implies that sea level fell from at least −14 m at 102.6 ± 0.5 ka, at the end of 5c, which is consistent in timing (103 ± 2 ka) and magnitude with the sea level record from the Red Sea (Rohling et al., 2009). MIS 5a timing based on isotope curves is $83_{-3}^{+1.5}$ ka, close to the timing of the second 5a peak in Lambeck and Chappell (2001).

Oakley et al. (2018) correlated terraces south of Kaikōura with the multiple peaks during MIS 5c and 5a reported from the Huon Peninsula (Lambeck and Chappell, 2001) but multiple terrace forming events during individual stages are not otherwise reported and levels are not entirely consistent with regional records. I adopt a single age and elevation for MIS5c of 103 ± 1 ka and $-12.6_{-2}^{+6.6}$ m RSL respectively.

MIS 5a is assigned an age range from 78 to 85 ka, with a peak probability at 83 ka, and an elevation of −14 ± 2 m RSL.

5.3.3. MIS 3

MIS3 is the most difficult sea level to define because it is only present above modern sea level along tectonically uplifted shorelines. MIS3 sea levels are commonly considered to have remained below an RSL of −50 m, based on ice volume equivalent sea level functions derived from coral records (e.g., Lambeck and Chappell, 2001). However, recent work has suggested that the Laurentide ice sheet was dramatically reduced in extent during MIS 3 and that global mean sea level reached as high as 38 m, even as late as 35 ka during this period (Pico et al., 2017; Dalton et al., 2019). This is broadly consistent with the timing and elevation of sea level scaled from oxygen isotope records, which indicate that MIS3 sea level rose to < 40 m during at least 4 excursions related to warming in Antarctica (Siddall et al., 2008), beginning 59 ka and may have reached as high as −20 m at 57 ka (Fig. 3 in Siddall et al., 2008).

Global mean sea levels relate to relative sea level through glacio-hydro-isostatic effects (changes in ice and water loading – see summary in Rovere et al. (2016)). These effects vary depending on location but in the mid-latitudes many areas adjacent to continental shelves report higher relative sea levels, e.g., the southwestern Atlantic coast (Salvaterra et al., 2017; Dillenburg et al., 2019), the South China Sea area (Hanebuth et al., 2006; Tanabe et al., 2006; Pico et al., 2016), the Gulf of Mexico (Simms et al., 2009), South Africa (Cawthra et al., 2018) and Australia (Cann et al., 1988).

The Australian site, located in a similar glacio-hydro-isostatic setting to the Kaikōura study site (e.g., Fig. 1 in Mitrovica and Milne, 2002), experienced relative sea levels of −22 m. Marine sediment on an MIS 3 terrace at Motunau Beach (85 km south of Kaikōura, similar elevation to T4) returned an IRSL age of 54 ± 6 ka (Oakley et al., 2017).

I therefore adopt an MIS3 sea level of -22_{-3}^{+5} m at 59_{-11}^{+3} ka.

6. Late Pleistocene fault geometry and slip rates

6.1. Fault geometry, slip and slip rates

The rotation model used here provides new insight into the geometry, slip and slip rates on the fault underlying the Kaikōura Peninsula. The fault geometry calculated from the model is summarized in Table 2. Correlating each of the three lower terraces with a major highstand (per the regional sea level curve described above) yielded terrace radii within 0.4–1.5% of the age-constrained T1 radius (19.46 ± 1.1 km).

Model fits to observed terrace levels were good; the maximum δZ of 2.7 times the error margin related to MIS 5a, which had been assigned error limits of only 2 m. The preferred model implies that slip accumulation since MIS 3 totals 232 ± ~70 m; this is a relatively large proportion of the total calculated slip of 386 ± ~20 m since MIS-5e. This in turn implies an increase in slip rates from 2.3 ± 1.5 mm/yr to 4.1 ± 1.3 mm/yr since MIS3 (Fig. 8a). However, a uniform slip rate of 3.2 ± 1.5 is equally likely because of the sensitivity of the model to certain input parameters that are explored below.

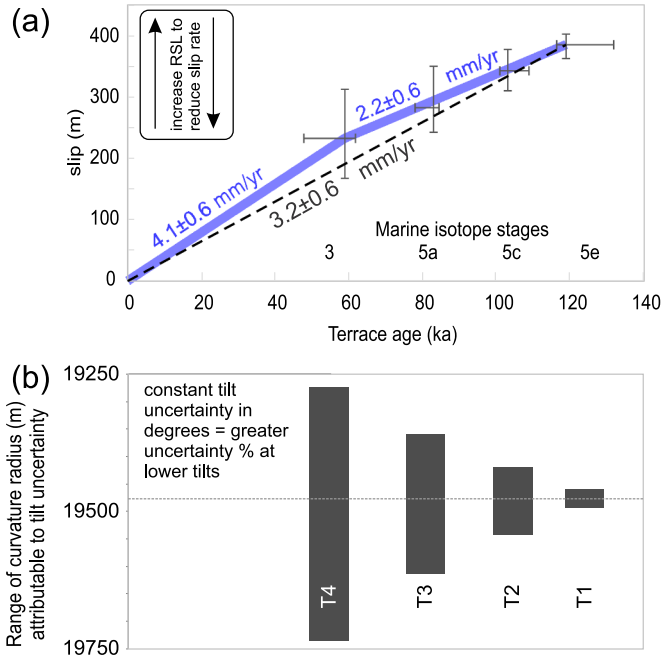

Fig. 8. a) Slip rates based on Monte Carlo analysis of age-tilt relationships using a regional sea-level curve. The increasing error margins for calculated slip of younger terraces is caused by using constant measurement error margins in degrees for all tilt measurements, as shown in b). As noted on (a), an apparent increase in slip rates would be removed if sea level was slightly higher than accounted for during MIS 3, 5a and 5c.

Note that this study inherently documents only dip-slip, so conservatively slip rates derived here represent minimum values. If the fault has a dextral oblique component and accommodates slip parallel to the relative motion vector, the net slip rate could be greater. However, historical seismicity within a few kilometers of the peninsula, both before and after the Kaikōura earthquake, along the coast and offshore, is dominated by thrusting at 13–15 km depth, with only a small component of strike slip (e.g., Reyners et al., 1997, see Fig. 1).

6.2. Model sensitivity to input parameters

The measurement uncertainties in model parameters are addressed

Table 2
Calculated slip history for terraces based on correlation with the regional sea-level curve. Error estimates are 95% confidence. Highest and lowest values of radii and fit are bolded. Late Holocene slip rate from beach uplift shown for comparison.

Terrace	RSL (m)	RSL +	RSL-	Tilt	Radius (mode)	Slip (mode)	Age	Age +	Age −	MIS stage	Fit (δZ)
Unit	m	m	m	deg	km	m	ka	ka	ka		
1	+2.1	1	1	1.12	18.3–20.6 (19.5)	364–403 (386)	119	13	2.5	5e	1.65
2	−12.6	6.6	2	1.00	18.5–21.0 (19.6)	311–378 (343)	103	6	2	5c	−1.54
3	−14	2	2	0.87	17.9–20.4 (19.2)	244–350 (283)	83	1.5	5	5a	2.7
4	−22	5	3	0.71	18.3–21.3 (19.6)	168–314 (232)	59	3	11	3	−0.83
Average											−0.47-1.72 (0.46)
Implied ancient slip rate											2.2 ± 1.5 mm/yr (0.99)
Implied present slip rate											4.1 ± 1.3 mm/yr
Probable uniform slip rate											3.2 ± 1.5 mm/yr
Holocene slip rate											$2.7_{-0.4}^{+0.7}$ mm/yr

by assigning distributions around a mean and incorporating these distributions in a Monte Carlo model. However, the assumptions listed in Table 1 also contribute to the modelled results.

The most important assumption is that all terraces are rotating above a single fault. The calculated radius of curvature of that fault, and its measured tilt, are the primary factors that govern the slip estimates. Even with relatively small assigned error bars, the calculated radius of curvature is most sensitive to the fault's location, given as distance from the peninsula. The assigned error bars only account for possible changes in position of up to a kilometer either side of the estimated trace. This is clearly an informed choice, model driven, and in fact, a priori, a range of options are feasible for the fault location (as close as a within-shelf location [e.g. Clark et al. (2017)]; as distant as the Kekerengu Bank) and fault dip (c.30–60°). Rotation of the peninsula above a fault located at a greater distance from the peninsula (e.g., the Kekerengu Bank Fault) requires unfeasibly high slip rates to match the observed terrace levels. Conversely, the long-term rotation of the Kaikōura Peninsula can be matched with an intra-shelf fault of low dip (e.g., Clark et al., 2017), albeit with a small increase in modelled slip rates. However, the strike of the Point Kean fault is significantly more easterly than the strike of the planes that define the terraces, which would imply a dextral oblique component along the Point Kean Fault and further drive up the net slip rates.

Apart from fault location, the radius of curvature is most sensitive to the selection of relative sea levels for the terraces. A deeper RSL at MIS3 would require either a much larger radius of curvature for that terrace than any other, adversely affecting the model fit, or a commensurately deeper RSL for all other terraces, resulting in increased slip rates. In contrast, the adopted RSL yields a good match for radius of curvature and slip rate across the full flight of terraces, even though it suggests a modest increase in slip rates post MIS 3. Those slip rates could be reduced to constant slip rates if high stands were slightly higher than used here during MIS 5c-3.

The next most influential parameter is the tilt of the terraces (Fig. 8b). The limitations of measurement are given in constant degrees, which equates to larger percentage error for lower tilt surfaces. Reducing that error margin would imply false confidence.

7. Holocene slip rates

7.1. Beach ridges and earthquake uplift

The Holocene beach ridges that fringe Kaikōura Peninsula provide information about Holocene tectonic uplift events. McFadgen's (1987) trenches across the Holocene beach ridges (Section 3.3) yielded a radiocarbon chronology, recalculated with up-to-date decay constants for this study https://www.elsevier.com/wps/find/journaldescription.cws_home/503362?generatepdf=true (Bruce McFadgen, personal communication), (Table 3). The chronology records new beach accretion episodes at 418–756 CE (beach 3), 1415–1699 CE (beach 2) and 1702–1838 CE (beach 1 – the pre-2016 modern beach). Details of the OxCal derivation of these dates are provided in the supplementary information and the dates are integrated into a graphic summary of beach accretion and earthquake events at Kaikōura (Fig. 9).

Comparison of the dated beach forming events with the late Holocene sea level curve for New Zealand (Hayward et al., 2016) (BE1, BE2 on Fig. 9) suggests that beaches 2, 3 and 4 are all consistently offset relative to the New Zealand Holocene sea level curve. This consistency implies that beaches 2 and 3 did not form in response to tectonic uplift (c.f. McFadgen, 1987; Barrell, 2015) but simply at intervals of stable sea level. The importance of sea-level stability for new beach inception is emphasized because shells deposited during accumulation of beaches 3 and 4 ranged several hundred years younger than the onset of sea level fall to a lower level, indicating that beach accretion continued until a new beach stabilized at the lower sea level (Fig. 9). In this way, new beach development follows more closely on a rapid fall than on a slow

Table 3
Radiocarbon and other age constraints on beach forming events and modelled beach forming event ages (bold).

NZ sample No.	CRA ^{14}C yrs. BP	δ^{13}C	Material dated	Significance	Modelled earliest date (CE, 68.2%)	Modelled latest date (CE, 68.2%)	Modelled earliest date (CE, 95.4%)	Modelled latest date (CE, 95.4%)
Relative sea level fall beaches 2–1 (eustatic rise, earthquake)					**1758**	**1831**	**1702**	**1838**
NZ3154	143 ± 58	−27.3	Description as above	Re-date of NZ1926. As above	1670	1738	1655	1816
NZ1926	297 ± 62	−26.6	Organic matter from bottom peat layer of old lagoon deposit, beneath beach barrier (B1), on mudstone shore platform.	Peat accumulation following uplift of B3 – minimum age for uplift of B3, max age for inception of B2	1558	1791	1506	1800
Sea level fall beaches 3–2					**1463**	**1608**	**1415**	**1700**
NZ6472	871 ± 40	1.2	Shells (*Haliotis iris* – the NZ paua or abalone)	Youngest age for accretion of B3 – max age for uplift of B3	1420	1491	1346	1529
NZ6744	1676 ± 29	1.52	Shells (Protothaca sp., Turbo smaragda)	Oldest age for accretion of B3 – min age for uplift of B4	674	764	630	815
Sea level fall – beaches 4–3					**509**	**692**	**420**	**757**
NZ6765	1932 ± 34	0.96	Shells (*Protothaca* sp.)	Youngest age for accretion of B4, max age for uplift of B4				
				Sea level fall from Hayward et al. (2016)	−532	−282	−654	−161
Sea level stabilization or (probable) earthquake					−1155	−580	−1286	−362
NZ6779	3354 ± 27	1.79	Shells (Turbo smaragda)	Old foreshore inland of B4, max age for inception of B4	−1326	−1188	−1383	−1121

one (compare beach-forming events BE1 and BE2 on Fig. 9), and thus might be expected to follow rapidly after an uplift event. During the intervening period between the start of sea level fall and the inception of a new beach, material continues accreting to the older beach, presumably during storms.

The highest (beach 4) and lowest (beach 1) are the only beaches that depart from a close age-elevation relationship with Holocene sea level. The circumstances under which beach 4 formed are not clear, but

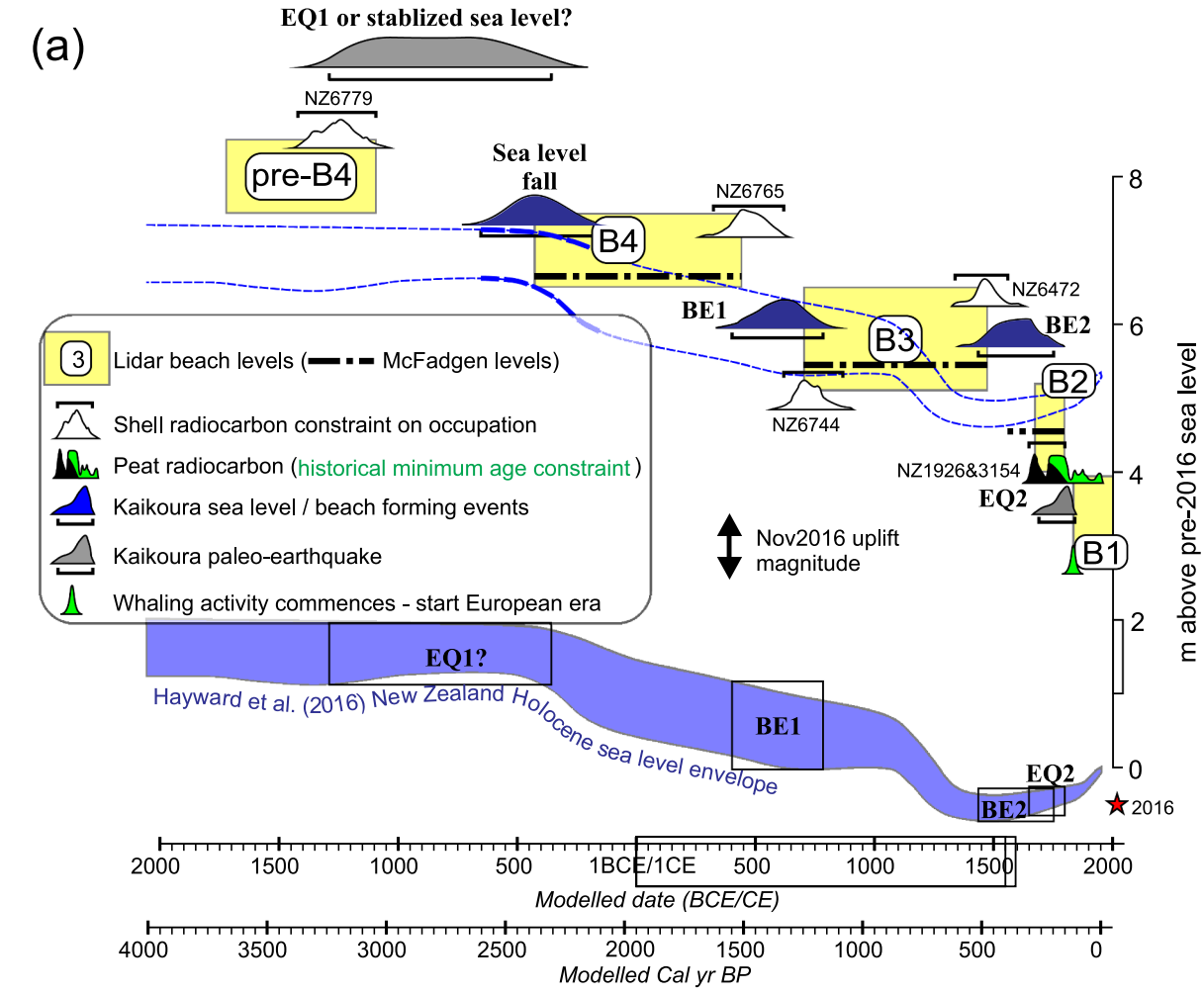

(caption on next page)

Fig. 9. A) age-elevation plot for the Kaikōura Peninsula, based on OxCal modelling of existing radiocarbon age determinations (McFadgen, 1987). Note close correlation between late Holocene sea level curve (Hayward et al., 2016) and the elevation age relationships of beaches 2–4. BE – Beach establishment; EQ – Earthquake. B) Compilation of regional paleoseismic ages for faults, ordered from north to South. Grey dashed rectangles delineate 500-year periods beginning with the 2016 earthquake, and show the number (n =) of paleoseismic or historic earthquakes that have > 50% probability of rupture having occurred within the interval. The most recent interval shows n based on future recognition of complex rupture in the 2016 earthquake, and without recognition of complex rupture (in parentheses). Two other possible complex events are highlighted in red, one of which involves the Kaikōura Peninsula Fault. Black arrows show Alpine Fault (AF) earthquakes. Paleoseismic data from: 1 - Langridge et al. (2011); 2 – Clark et al. (2015); 3 – Nicol and Van Dissen (2018); 4 – Bartholomew et al. (2014); 5 - Mason et al. (2006), Benson et al. (2001), McCalpin (1996); 6 - Van Dissen and Nicol (2009); 7 - Little et al. (2018); 8 - Van Dissen et al. (2006); 9 - Khajavi et al. (2016);10 - Hatem et al. (2019); 11 - This study; 12 - Howard et al. (2005). Note that the possible minor slip on the Vernon and Awatere faults in 1855 is based on contemporary accounts compiled and interpreted by Grapes and Holdgate (2014). (For interpretation of the references to colour in this figure legend, the reader is referred to the web version of this article.)

it may have formed either due to stabilization of sea level during the mid-Holocene high stand, or following tectonic uplift. The latter is preferred based on slip rates presented later. Beach 1 recorded a relative sea level fall as New Zealand's eustatic sea level rose in the 'Anthropocene' (Hayward et al., 2016); I interpret this as the only possible earthquake in the beach record other than the beach 4 uplift event. The OxCal modelled date for this possible earthquake, bracketed by the age of lagoonal peats below beach 1 and the establishment of permanent whaling in 1840, is 1702–1838 CE. The advanced development of beach 2 suggests that the event probably occurred toward the end of that period, around 1800 CE. Further detail is provided in the supplementary information.

7.2. Single event uplift implied by beach records

The evidence outlined above suggests that no more than two late Holocene earthquakes caused pre-November 2016 uplift of the Kaikōura Peninsula. The coseismic uplift, if any, that initiated beach 4 cannot be constrained, but the coseismic uplift that probably resulted in a relative sea level fall in the late 18th century and accretion of beach 1 can be assessed. Around most of the peninsula, beach 1 stands ~3.5 m above 2016 sea level (Fig. 9). The broad coincidence between late Holocene sea levels and beach relative elevations implies that the beaches maintained a relatively consistent elevation relative to sea level. The pre-2016 height (~3.45 m) provides a minimum estimate for this parameter because post-18th century beaches have experienced a different environment of accretion. Firstly, the modern beaches are walked on and potentially lowered by the million or more tourists (and ~60 geology students) who visit the peninsula each year (Fairweather and Simmons, 1998) and walk through the slippery gravel on the beach crest. Perhaps more importantly, the 18th century uplift event may have substantially reduced the wave energy acting at the beach. I therefore adopt a broadly-defined pre-18th century beach height that encompasses a range from the minimum pre-2016 beach height to the c.3.9 m elevation difference between the beach crest and the 18th century RSL, with associated error margins. This gives a beach height relative to RSL at formation of 3.7 ± 0.4 m. The average elevation of beaches 2, 3 and 4 relative to their RSL at formation is 5 ± 0.45 m. The difference implies an 18th century coseismic vertical displacement of 1.35 ± 0.25 m.

7.3. Model Late Holocene single-event and cumulative slip

The slip to uplift ratio at the McFadgen (1987) site, implied by its model position above a listric fault of radius 19.5 ± 1.2 km, is about 3.28 ± 0.2:1. Applying that ratio to the 1.35 ± 0.25 m pre-whaling uplift determined above, and assuming dip-slip on the Kaikōura Peninsula Fault, yields single-event slip of 4.4 ± 0.9 m. This is generally consistent with the 3 m average displacement modelled on the Point Kean Fault by Clark et al. (2017), and on the off-shore thrust fault by Mouslopoulou et al. (2019), and well within the c.7 m maximum slip suggested by the latter. Applying the slip to uplift ratio to the 2016 coseismic uplift at the trench site yields an estimated slip of 3 m, consistent with Clark et al. (2017), and a total 7.7 ± 0.9 m of Late Holocene slip since establishment of beach 4.

7.4. Centennial to millennial slip rates

Apportioning the cumulative slip over the time between the inception of beach 4 at about 2370–3300 years ago (the youngest probable age for a pre-18th century earthquake) and pre-2016, would have yielded a millennial-scale late Holocene slip rate of only 1.6 ± 0.4 mm/yr (if beach 4 was uplifted by earthquake). If the 0.8–1.0 m of 2016 Kaikōura earthquake uplift is included (Clark et al., 2017), the late Holocene slip rate increases to $2.7_{-0.4}^{+0.7}$ mm/yr, similar to the model long-term slip rate.

8. Discussion

8.1. Regional structural context of the Kaikōura Peninsula Fault

The radius of curvature estimated for the Kaikōura Peninsula Fault's suggests that the dip decreases rapidly to the NW, such that it dips ~25–40° below the Kaikōura Peninsula compared with 60° at the shelf edge. In a regional cross section through the peninsula, its *average* position is not dissimilar to other interpretations of the offshore thrusting, including those proposed by Clark et al. (2017) and Mouslopoulou et al. (2019), despite their differences in fault position and strike (Fig. 1C). The shelf edge position and listric geometry are also consistent with similar structures like the Te Rapa Fault that are mapped further north of Kaikōura (Barnes and Audru, 1999).

Early cross sections through the offshore Marlborough region showed the Kekerengu Bank Fault dipping > 40° and merging with the subduction interface at c.8 km depth, while more inboard faults had steeper dips and merged with the plate boundary fault at greater depths (e.g., Fig. 12 in Barnes et al., 1998). However, the geometry inferred here for the Kaikōura Peninsula Fault, along with 1) the listric nature of the outer shelf faults revealed by seismic reflection profiles (Barnes and Audru, 1999), 2) the low seismogenic-depth dips implied by fault source models (Clark et al., 2017; Mouslopoulou et al., 2019), and 3) the best information on the depth to the subduction interface (Williams et al., 2013) implies that most of the deformation is taking place well above and sub-parallel to the subduction interface (Fig. 1C). An analogous situation is the Timor Trough, which merges along strike with the Java subduction trench but itself represents a foredeep, rather than the trace of a subduction zone (Duffy and Sandiford, 2017). The northern Australian continental basement that links to any subducting slab is buried at several km depth (e.g., Audley-Charles, 2004). Like offshore Marlborough (Barnes et al., 1998), the Timor Trough is marked by weak extension in the downwarped continental margin (Saqab and Bourget, 2015) and a weakly deformed trench fill (Breen et al., 1986; Poynter et al., 2013). However, in the Timor example, thrusting is well-imaged to depth by industry 3D seismic reflection and occurs along a low-angle fault (Poynter et al., 2013; Baillie et al., 2019) with listric thrusts in the hanging wall (Martinez Duran et al., 2019).

The fault models shown in Fig. 1C suggest that the seismogenic offshore thrust fault truncates the Seaward segment of the Hope Fault close to the intersection of the Hope Fault with the Kowhai fault and

Jordan Thrust. This further implies that the offshore thrust is effectively a footwall splay of the Jordan Thrust and that the Seaward segment of the Hope Fault lies within that block and accommodates the dextral component of slip imparted by displacement on the more rapidly slipping segments of the Hope Fault. This is consistent with Pettinga et al. (2019), who report that the along strike transition from the Conway/Fyffe segment of the Hope Fault to its Seaward segment is marked by an abrupt transition to transpression, substantial widening of the fault zone, and minor slip on thrust flaps during the Kaikōura earthquake.

It is not clear how the putative Kaikōura Peninsula Fault interacts with faults further south, like the Conway Ridge Fault (Fig. 1). However, it probably involves inversion of EW fault systems of the North Mernoo Fault Zone on the Chatham Rise (Barnes, 1994). Analogous inherited structures in North Canterbury display clear examples of oppositely vergent fold and thrust development at breached normal relays either side of EW normal faults (Campbell et al., 2012).

8.2. Earthquake behavior

Well-documented multi-fault ruptures in New Zealand (Quigley et al., 2012; Hamling et al., 2017) and elsewhere (Simons et al., 2002; Sieh et al., 1993; Fletcher et al., 2016) have renewed focus on whether faults typically rupture together or in isolation, a question that has been addressed in New Zealand using spatio-temporal paleoseismic data compilations (Little et al., 2018; Hatem et al., 2019) and stress modelling (Quigley et al., 2019). Regional paleoseismic compilations (Little et al., 2018; Hatem et al., 2019) have highlighted the coincidence between the timing of paleo-earthquakes on the Kekerengu, Hope (represented here by Hurunui and Conway segments) and Alpine Faults (Fig. 9B), which seem to indicate increased seismicity over the last few hundred years.

Recent uplift events at the Kaikōura Peninsula align well with the period of increased seismicity that covers the last three major events or series of events to rupture the Marlborough Fault system. The intervals between paleo-earthquakes on the Hope, Kekerengu and Kaikōura Peninsula Faults are too small to resolve with the radiocarbon dating, and uplift above the Kaikōura Peninsula Fault correlates with slip on these faults in the late 18th to early 19th century (Hatem et al.'s Sequence 1) and in the 2016 Kaikōura earthquake.

The temporal and kinematic association of increased regional seismicity with slip on the previously quiescent Kaikōura Peninsula Fault is suggestive of keystone fault operation (e.g., Fletcher et al., 2016; Quigley et al., 2019), a concept already speculatively advanced to account for the large extent and slip characteristics of the Kaikōura Earthquake (Hamling et al., 2017). This may have been a multi-fault keystone system. For example, the Papatea Fault is remarkably steep, with a dip close to vertical (Diederichs et al., 2019), even steeper than the dips of up to 75° for the probable keystone Charing Cross Fault in the Canterbury earthquake sequence (Quigley et al., 2019). As discussed above, both earthquake slip models indicate that the Seaward segment of the Hope Fault and the Papatea fault both sole onto the Kaikōura Peninsula Fault at depth (Fig. 1c) (e.g., Mouslopoulou et al., 2019). Differential lidar analysis and field observations show that the Papatea fault extruded to the southeast (Stirling et al., 2017; Diederichs et al., 2019), with estimated displacement vectors almost exactly aligned with the dip direction of the Kaikōura Peninsula Fault (Diederichs et al., 2019). This suggests that the Kaikōura Peninsula Fault, in conjunction with the Papatea Fault, may introduce geometric incompatibility (e.g., Gabrielov et al., 1996) that inhibits the transfer of slip from the Hope Fault to the Kekerengu Fault. This incompatibility may have led to accumulation of a slip deficit on the Papatea Fault that was resolved by feeding of the Jordan-Papatea block toward the Kaikōura Peninsula Fault. A low slip tendency on the Kaikōura Peninsula Fault due to its steep dip in the upper crust may have facilitated the development of super-critical stresses on other system faults, during the long interseismic interval on the Kaikōura Peninsula Fault.

Observations from diverse settings, including the MFS (Knuepfer, 1992), stable continental regions (Clark et al., 2012) and other plate boundary settings (Dolan et al., 2007), along with equivalent results from numerical models (Ben-Zion et al., 1999), suggest that fault systems may respond to seismic loading by switching modes between 1) clusters of seismic events that encompass the largest events on the system, and 2) periods of low moment release during small to moderate earthquakes. The clustering of seismicity in this case may be indicative of mode switching driven by keystone faulting.

8.3. Coastal uplift mechanisms

Many studies have considered the diversity of mechanisms of coastal uplift at convergent margins. In places including but not limited to the Hikurangi Margin (Berryman, 1993; Barnes et al., 2002; Litchfield et al., 2020), the junction of the Yakutat Terrane the Aleutian trench in the Gulf of Alaska (Plafker and Rubin, 1978; Fruehn et al., 1999), the north coast of Timor in Eastern Indonesia (Cox, 2009) and coastal Chile's Arauco Peninsula (Melnick et al., 2009), large scale convergent tectonics provide a context for uplift, but coseismic uplift by upper plate reverse faulting is required to reconcile short wavelength variations in uplift timings and rates. The Kaikōura Peninsula provides another example, in keeping with the rest of the Hikurangi margin (Mountjoy and Barnes, 2011), where a high rate of uplift is associated with a fault that reaches the surface within 8 km of the shoreline.

Hikurangi examples such as the Mahia and Kaikōura Peninsulas also illustrate the importance of listric thrusts and fault interactions for the geomorphic development and earthquake hazard of the New Zealand plate boundary. The marine terraces of the Mahia Peninsula are uplifted and folded in the hanging wall of the listric Lachlan Fault (Berryman, 1993; Barnes et al., 2002). They are actively folding (Berryman, 1993), possibly driven by backthrusting (Barnes et al., 2002), and the higher terraces on the seaward side of the peninsula are notably flatter than their landward equivalents. These flat terraces overlie the backlimb of a west-vergent backthrust fold imaged in seismic reflection surveys offshore of the peninsula (Barnes et al., 2002). In contrast, the folding of the Kaikōura Peninsula does not appear to be active and terraces remain flat over mapped bedrock folds (Rattenbury et al., 2006). Where active folds have previously been inferred (c.f. Campbell et al., 2005), they are revealed by lidar to be short wavelength humps that follow the buried outcrop of a resistant, folded limestone. The relatively small thickness of sediments and presence of shallow bedrock may be a factor in the relative simplicity of uplift of the Kaikōura peninsula compared with Mahia.

8.4. Sea level curves

In common with other coastal uplift studies, this study has been critically dependent on a model of sea level history. It uses the highest reasonable RSL for MIS 3, based on regional observations and on the fact that deeper RSLs create irreconcilable individual determinations of fault radii and completely improbable post-MIS 3 slip rates. This decision is supported by; (i) the results of the recent studies demonstrating substantially higher global mean sea level during MIS 3 (Pico et al., 2016; Pico et al., 2017; Dalton et al., 2019), (ii) Recent work south of Kaikōura that used an oxygen isotope sea level curve with an MIS 3 RSL of 35 ± 18 m (Oakley et al., 2017; VanderLeest et al., 2017). Like this study, VanderLeest et al. (2017) obtained a slightly higher uplift rate since MIS 3 but within error of older terraces. (iii) Older work in New Zealand's North Island (Berryman, 1993) that predated interpretations of deeper sea levels in MIS 3 and yielded sensible results. However, the long association of MIS 3 with large ice volumes and low sea levels means that many studies globally have used low RSL estimates, with important implications for uplift rates. Recent studies have documented apparently anomalous MIS 3 to recent uplift rates in Iran (Normand et al., 2019) and Chile (Binnie et al., 2016; González-Alfaro et al., 2018)

among others, while some studies that argued for high MIS 3 sea levels in the Mediterranean (Doğan et al., 2012a) attracted stiff opposition despite abundant evidence (Doğan et al., 2012b). Many coastal uplift studies will clearly need to be revisited to redress misinterpretations caused by misunderstanding of MIS 3 sea level. For the North Canterbury and Marlborough regions of New Zealand, the coherence of calculated fault radii strongly supports an MIS 3 sea level of no deeper than 22 m below modern sea levels.

9. Conclusions

The model explored here accounts for uplift of the Kaikōura Peninsula since the MIS 5e, by slip along the Kaikōura Peninsula Fault, located about 8 km offshore at the base of the shelf edge.

1. The fault probably soles into a shallow dipping decollement that splays off from the Jordan Thrust and has fundamentally altered the kinematics of the seaward segment of the Hope Fault.
2. The fault slip occurred at rates between 2.3 ± 1.5 mm/yr and 4.1 ± 1.3 mm/yr; a possible increase toward the higher rates since MIS3 is no more likely than a constant slip rate, which would only require slightly higher sea levels at MIS3, 5a and 5c.
3. Most of the Late Holocene slip has occurred in two events within the last 500 years, which occurred within a period of relatively intense seismicity in the MFS, based on the regional paleoseismic record.
4. Within the limits of data, Late Holocene slip rates that account for the 2016 earthquake are equivalent to long-term rates. The 2016 earthquake therefore seems to have resolved a measurable slip deficit that existed prior to the earthquake.
5. The coherence of fault radius and slip rates based on multiple terraces lends support to a growing understanding that sea levels ranged higher than −40 m during MIS 3, which has implications for supposed post-MIS 3 accelerated uplift suggested elsewhere.

CRediT authorship contribution statement

Brendan Duffy:Conceptualization, Formal analysis, Writing - original draft, Writing - review & editing.

Declaration of competing interest

The author declare that they have no known competing financial interests or personal relationships that could have appeared to influence the work reported in this paper.

Acknowledgements

The lidar data used here was provided to me by the GIS team at Environment Canterbury in mid-2013. The same data can be obtained from http://opentopo.sdsc.edu/lidarDataset?opentopoID=OTLAS.122016.2193.1. Focal mechanisms in Fig. 1 are from the Geonet catalog (https://github.com/GeoNet/data/tree/master/moment-tensor), last accessed 4 August 2017. I thank Bruce McFadgen for the recalculated radiocarbon ages for the Kaikōura beaches. I also thank multiple reviewers for constructive reviews of several iterations of this study that have all contributed to improving the final manuscript. The improvements are theirs, the mistakes mine.

Appendix A. Supplementary data

Supplementary data to this article can be found online at https://doi.org/10.1016/j.tecto.2020.228460.

References

Amos, C.B., Burbank, D.W., Nobes, D.C., Read, S.A.L., 2007. Geomorphic constraints on listric thrust faulting: implications for active deformation in the Mackenzie Basin, South Island, New Zealand. Journal of Geophysical Research: Solid Earth 112, B03S11.
Audley-Charles, M.G., 2004. Ocean trench blocked and obliterated by Banda forearc collision with Australian proximal continental slope. Tectonophysics 389, 65–79.
Baillie, P., Keep, M., Duran, P.M., Carrillo, E., Duval, G., 2019. Broadband seismic imaging around the Banda Arc: changes in the anatomy of offshore fold-and-thrust belts. Geol. Soc. Lond., Spec. Publ. 490, SP490–2018-2141.
Barnes, P.M., 1994. Inherited structural control from repeated Cretaceous to recent extension in the North Mernoo Fault Zone, western Chatham Rise, New Zealand. Tectonophysics 237, 27–46.
Barnes, P.M., Audru, J.-C., 1999. Recognition of active strike-slip faulting from high-resolution marine seismic reflection profiles: Eastern Marlborough fault system, New Zealand. Geol. Soc. Am. Bull. 111, 538–559.
Barnes, P.M., De Lépinay, B.M., Collot, J.-Y., Delteil, J., Audru, J.-C., 1998. Strain partitioning in the transition area between oblique subduction and continental collision, Hikurangi margin, New Zealand. Tectonics 17, 534–557.
Barnes, P.M., Nicol, A., Harrison, A., 2002. Late Cenozoic evolution and earthquake potential of an active listricthrust complex above the Hikurangi subduction zone, New Zealand. Geol. Soc. Am. Bull. 114, 1379–1405.
Barrell, D., 2015. General Distribution and Characteristics of Active Faults and Folds in the Kaikōura District, North Canterbury. GNS Science Consultancy Report 2014/210.
Barth, N.C., Toy, V.G., Langridge, R.M., Norris, R.J., 2012. Scale dependence of oblique plate-boundary partitioning: new insights from LiDAR, central Alpine fault, New Zealand. Lithosphere 4, 435–448.
Bartholomew, T.D., Little, T.A., Clark, K.J., Van Dissen, R., Barnes, P.M., 2014. Kinematics and paleoseismology of the Vernon Fault, Marlborough Fault System, New Zealand: implications for contractional fault bend deformation, earthquake triggering, and the record of Hikurangi subduction earthquakes. Tectonics 33, 1201–1218.
Benson, A., Little, T.A., Van Dissen, R., Hill, N., Townsend, D.B., 2001. Late Quaternary paleoseismic history and surface rupture characteristics of the eastern Awatere strike-slip fault, New Zealand. Geol. Soc. Am. Bull. 113, 1079–1091.
Ben-Zion, Y., Dahmen, K., Lyakhovsky, V., Ertas, D., Agnon, A., 1999. Self-driven mode switching of earthquake activity on a fault system. Earth Planet. Sci. Lett. 172, 11–21.
Berryman, K.R., 1993. Distribution, Age, and Deformation of Late Pleistocene Marine Terraces at Mahia Peninsula, Hikurangi Subduction Margin, New Zealand. 12. pp. 1365–1379.
Binnie, A., Dunai, T.J., Binnie, S.A., Victor, P., González, G., Bolten, A., 2016. Accelerated late quaternary uplift revealed by 10Be exposure dating of marine terraces, Mejillones Peninsula, northern Chile. Quat. Geochronol. 36, 12–27.
Blakemore, A.G., Murray-Wallace, C.V., Lachlan, T.J., 2014. First recorded evidence of subaqueously-deposited Late Pleistocene interstadial (MIS 5c) coastal strata above present sea level in Australia. Mar. Geol. 355, 377–383.
Breen, N.A., Silver, E.A., Hussong, D.M., 1986. Structural styles of an accretionary wedge south of the island of Sumba, Indonesia, revealed by Sea Marc II side scan sonar. Geol. Soc. Am. Bull. 97, 1250–1261.
Bull, W.B., Cooper, A.F., 1986. Uplifted marine terraces along the Alpine Fault, New Zealand. Science 234, 1225–1228.
Campbell, J.K., Tonkin, P., Bradshaw, J.D., 2005. Structure and tectonics of the Kaikōura Peninsula. In: Pettinga, J.R., Wandres, A.M. (Eds.), Field Trip Guides, Geological Society of new Zealand 50 Annual Conference, Kaikōura, New Zealand. 119B. Geological Society of New Zealand Misc. Publ, pp. 111–127.
Campbell, J., Pettinga, J., Jongens, R., 2012. The tectonic and structural setting of the 4th September 2010 Darfield (Canterbury) earthquake sequence, New Zealand. N. Z. J. Geol. Geophys. 55, 155–168 (Canterbury, New Zealand, 2010-2011 earthquake sequence).
Cann, J.H., Belperio, A.P., Gostin, V.A., Murray-Wallace, C.V., 1988. Sea-level history, 45,000 to 30,000 yr B.P., inferred from Benthic foraminifera, Gulf St. Vincent, South Australia. Quat. Res. 29, 153–175.
Caputo, R., 2007. Sea-level curves: perplexities of an end-user in morphotectonic applications. Glob. Planet. Chang. 57, 417–423.
Cawthra, H.C., Jacobs, Z., Compton, J.S., Fisher, E.C., Karkanas, P., Marean, C.W., 2018. Depositional and sea-level history from MIS 6 (termination II) to MIS 3 on the southern continental shelf of South Africa. Quat. Sci. Rev. 181, 156–172.
Chiswell, S.M., Schiel, D.R., 2001. Influence of along-shore advection and upwelling on coastal temperature at Kaikōura Peninsula, New Zealand. N. Z. J. Mar. Freshw. Res. 35, 307–317.
Clark, D., McPherson, A., Van Dissen, R., 2012. Long-term behaviour of Australian stable continental region (SCR) faults. Tectonophysics 566, 1–30.
Clark, K.J., Hayward, B.W., Cochran, U.A., Wallace, L.M., Power, W.L., Sabaa, A.T., 2015. Evidence for Past Subduction Earthquakes at a Plate Boundary with Widespread Upper Plate Faulting: Southern Hikurangi margin, New Zealand. Bull. Seismol. Soc. Am. 105, 1661–1690. https://doi.org/10.1785/0120140291.
Clark, K.J., Nissen, E.K., Howarth, J.D., Hamling, I.J., Mountjoy, J.J., Ries, W.F., Jones, K., Goldstien, S., Cochran, U.A., Villamor, P., Hreinsdóttir, S., Litchfield, N.J., Mueller, C., Berryman, K.R., Strong, D.T., 2017. Highly variable coastal deformation in the 2016 MW7.8 Kaikōura earthquake reflects rupture complexity along a transpressional plate boundary. Earth Planet. Sci. Lett. 474, 334–344. https://doi.org/10.1016/j.epsl.2017.06.048.
Clement, A.J.H., Whitehouse, P.L., Sloss, C.R., 2016. An examination of spatial variability in the timing and magnitude of Holocene relative sea-level changes in the New

Zealand archipelago. Quat. Sci. Rev. 131 (Part A), 73–101.
Cooper, A.F., Kostro, F., 2006. A tectonically uplifted marine shoreline deposit, Knights Point, Westland, New Zealand. N. Z. J. Geol. Geophys. 49, 203–216.
Cowan, H.A., 1992. Structure, Seismicity and Tectonics of the Porters Pass-Amberley Fault Zone, North Canterbury, New Zealand. Department of Geological Sciences University of Canterbury, Christchurch, New Zealand.
Cox, N.L., 2009. Variable Uplift from Quaternary Folding Along the Northern Coast of East Timor, Based on U-Series Age Determinations of Coral Terraces. Department of Geological Sciences. Brigham Young University, Provo, Utah, pp. 151.
Cutler, P.M., Cutler, K.B., Edwards, R.L., Taylor, F.W., Cheng, H., Adkins, J., Gallup, C.D., Burr, G.S., Bloom, A.L., 2003. Rapid sea-level fall and deep-ocean temperature change since the last interglacial period. Earth Planet. Sci. Lett. 206, 253–271.
Dalton, A.S., Finkelstein, S.A., Forman, S.L., Barnett, P.J., Pico, T., Mitrovica, J.X., 2019. Was the Laurentide Ice Sheet significantly reduced during Marine Isotope Stage 3? Geology 47, 111–114.
DeMets, C., Gordon, R.G., Argus, D.F., 2010. Geologically current plate motions. Geophys. J. Int. 181, 1–80.
Diederichs, A., Nissen, E.K., Lajoie, L.J., Langridge, R.M., Malireddi, S.R., Clark, K.J., Hamling, I.J., Tagliasacchi, A., 2019. Unusual kinematics of the Papatea fault (2016 Kaikōura earthquake) suggest anelastic rupture. Sci. Adv. 5, eaax5703.
Dillenburg, S.R., Barboza, E.G., Rosa, M.L.C.C., Caron, F., Cancelli, R., Santos-Fischer, C.B., Lopes, R.P., do Nascimento Ritter, M., 2019. Sedimentary records of Marine Isotopic Stage 3 (MIS 3) in southern Brazil. Geo-Mar. Lett. https://doi.org/10.1007/s00367-019-00574-2.
Doğan, U., Koçyiğit, A., Varol, B., Özer, İ., Molodkov, A., Zöhra, E., 2012a. MIS 5a and MIS 3 relatively high sea-level stands on the Hatay–Samandağ Coast, Eastern Mediterranean, Turkey. Quat. Int. 262, 65–79.
Doğan, U., Koçyiğit, A., Varol, B., Özer, İ., Molodkov, A., Zöhra, E., 2012b. Reply to the comments by Erdem Bekaroğlu on "MIS 5a and MIS 3 relatively high sea-level stands on the Hatay-Samandağ Coast, Eastern Mediterranean, Turkey". Quat. Int. 262, 84–87.
Dolan, J.F., Bowman, D.D., Sammis, C.G., 2007. Long-range and long-term fault interactions in Southern California. Geology 35, 855.
Duffy, B., 2014. Tilting of marine terraces above a listric thrust fault. In: 2014 GSA Annual Meeting Vancouver, British Columbia.
Duffy, B., 2017. Slip rate estimation from tilting of marine terraces above an offshore listric thrust fault, Kaikōura, New Zealand. In: Clark, K.J., Upton, P., Langridge, R., Kelly, K., Hammond, K. (Eds.), 8th International INQUA Meeting on Paleoseismology, Active Tectonics and Archaeoseismology (PATA). INQUA, Blenheim, New Zealand.
Duffy, B., Sandiford, M., 2017. Geology and Geomorphology of the Timor Trough and Relevance to Timor-Leste's Maritime Boundary: Invited Submission to the Permanent Court of Arbitration in the Hague. The University of Melbourne, Melbourne, pp. 24.
Dutton, A., Lambeck, K., 2012. Ice volume and sea level during the last interglacial. Science 337, 216–219.
Erslev, E.A., 1991. Trishear fault-propagation folding. Geology 19, 617–620.
Fairweather, J.R., Simmons, D.G., 1998. Estimating the Number of Visitors to Kaikōura over One Year by Developing a Vehicle Observation Method. Lincoln University, Canterbury, New Zealand (Tourism Research and Education Centre).
Fletcher, J.M., Oskin, M.E., Teran, O.J., 2016. The role of a keystone fault in triggering the complex El Mayor-Cucapah earthquake rupture. Nat. Geosci. 9, 303–307.
Fruehn, J., Von Huene, R., Fisher, M.A., 1999. Accretion in the wake of terrane collision: the Neogene accretionary wedge off Kenai Peninsula, Alaska. Tectonics 18, 263–277.
Gabrielov, A., Keilis-Borok, V., Jackson, D.D., 1996. Geometric incompatibility in a fault system. Proc. Natl. Acad. Sci. 93, 3838–3842.
Goded, T., Horspool, N., Canessa, S., Gerstenberger, M., 2017. Modified mercalli intensities for the M7.8 Kaikōura (New Zealand) 14 November 2016 earthquake derived from 'felt detailed' and 'felt rapid' online questionnaires. Bull. N. Z. Soc. Earthq. Eng. 50, 352–362.
González-Alfaro, J., Vargas, G., Ortlieb, L., González, G., Ruiz, S., Báez, J.C., Mandeng-Yogo, M., Caquineau, S., Álvarez, G., Del Campo, F., Del Río, I., 2018. Abrupt increase in the coastal uplift and earthquake rate since ~40 ka at the northern Chile seismic gap in the Central Andes. Earth Planet. Sci. Lett. 502, 32–45.
Grapes, R.H., Holdgate, G.R., 2014. Earthquake clustering and possible fault interactions across Cook Strait, New Zealand, during the 1848 and 1855 earthquakes. N. Z. J. Geol. Geophys. 57, 312–330.
Hails, J.R., Belperio, A.P., Gostin, V.A., 1984. Quaternary sea levels, northern Spencer Gulf, Australia. Mar. Geol. 61, 373–389.
Hamling, I.J., Hreinsdóttir, S., Clark, K., Elliott, J., Liang, C., Fielding, E., Litchfield, N., Villamor, P., Wallace, L., Wright, T.J., 2017. Complex multifault rupture during the 2016 Mw 7.8 Kaikōura earthquake, New Zealand. Science 356 (6334), eaam7194. https://doi.org/10.1126/science.aam7194.
Hanebuth, T.J.J., Saito, Y., Tanabe, S., Vu, Q.L., Ngo, Q.T., 2006. Sea levels during late marine isotope stage 3 (or older?) reported from the Red River delta (northern Vietnam) and adjacent regions. Quat. Int. 145–146, 119–134.
Hardy, S., Poblet, J., 1994. Geometric and numerical model of progressive limb rotation in detachment folds. Geology 22, 371–374.
Harris, R.A., 2011. The nature of the Banda arc–continent collision in the Timor Region. In: Brown, D., Ryan, P.D. (Eds.), Arc-Continent Collision. Springer, Heidelberg, Berlin, pp. 163–211.
Hatem, A.E., Dolan, J.F., Zinke, R.W., Van Dissen, R.J., McGuire, C.M., Rhodes, E.J., 2019. A 2000 Yr Paleoearthquake record along the Conway Segment of the Hope Fault: implications for patterns of Earthquake Occurrence in Northern South Island and Southern North Island, New Zealand. Bull. Seismol. Soc. Am. 109, 2216–2239.
Hayward, B.W., Grenfell, H.R., Sabaa, A.T., Cochran, U.A., Clark, K.J., Wallace, L., Palmer, A.S., 2016. Salt-marsh foraminiferal record of 10 large Holocene (last 7500 yr) earthquakes on a subducting plate margin, Hawkes Bay, New Zealand. Geol. Soc. Am. Bull. 128, 896–915.
Hearty, P.J., Hollin, J.T., Neumann, A.C., O'Leary, M.J., McCulloch, M., 2007. Global sea-level fluctuations during the last interglaciation (MIS 5e). Quat. Sci. Rev. 26, 2090–2112.
Hollingsworth, J., Ye, L., Avouac, J.-P., 2017. Dynamically triggered slip on a splay fault in the Mw 7.8, 2016 Kaikōura (New Zealand) earthquake. Geophys. Res. Lett. 44, 3517–3525.
Holt, W.E., Haines, A.J., 1995. The Kinematics of Northern South Island, New Zealand, Determined from Geologic Strain Rates. 100. pp. 17991.
Howard, M., Nicol, A., Campbell, J., Pettinga, J., 2005. Holocene paleoearthquakes on the strike-slip Porters Pass Fault, Canterbury, New Zealand. New Zealand Journal of Geology & Geophysics 48, 59–74.
Inkpen, R.J., Stephenson, W.J., Kirk, R.M., Hemmingsen, M.A., Hemmingsen, S.A., 2010. Analysis of relationships between micro-topography and short- and long-term erosion rates on shore platforms at Kaikōura Peninsula, South Island, New Zealand. Geomorphology 121, 266–273.
Khajavi, N., Langridge, R.M., Quigley, M.C., Smart, C., Rezanejad, A., Martín-González, F., 2016. Late Holocene rupture behavior and earthquake chronology on the Hope fault, New Zealand. GSA Bull. 128, 1736–1761.
Knuepfer, P.L.K., 1992. Temporal variations in latest Quaternary slip across the Australian- Pacific plate boundary, northeastern South Island, New Zealand. Tectonics 11, 449–464.
Lambeck, K., Chappell, J., 2001. Sea level change through the last glacial cycle. Science 292, 679–686.
Langridge, R.M., Campbell, J., Hill, N., Pere, V., Pope, J., Pettinga, J., Estrada, B., Berryman, K., 2003. Paleoseismology and Slip Rate of the Conway Segment of the Hope Faultat Greenburn Stream, South Island, New Zealand. 2003. pp. 46.
Langridge, R.M., Villamor, P., Basili, R., Almond, P., Martinez-Diaz, J.J., Canora, C., 2010. Revised slip rates for the Alpine fault at Inchbonnie: implications for plate boundary kinematics of South Island, New Zealand. Lithosphere 2, 139–152.
Langridge, R.M., Van Dissen, R., Rhoades, D., Villamor, P., Little, T., Litchfield, N., Clark, K., Clark, D., 2011. Five thousand years of surface ruptures on the Wellington Fault, New Zealand: implications for recurrence and fault segmentation. Bull. Seismol. Soc. Am. 101, 2088–2107.
Lanza, F., Chamberlain, C.J., Jacobs, K., Warren-Smith, E., Godfrey, H.J., Kortink, M., Thurber, C.H., Savage, M.K., Townend, J., Roecker, S., Eberhart-Phillips, D., 2019. Crustal fault connectivity of the Mw 7.8 2016 Kaikōura Earthquake constrained by aftershock relocations. Geophys. Res. Lett. 46, 6487–6496.
Le Béon, M., Suppe, J., Jaiswal, M.K., Chen, Y.-G., Ustaszewski, M.E., 2014. Deciphering cumulative fault slip vectors from fold scarps: Relationships between long-term and coseismic deformations in Central Western Taiwan. Journal of Geophysical Research: Solid Earth 119 (2013JB010794).
Litchfield, N.J., Campbell, J.K., Nicol, A., 2003. Recognition of active reverse faults and folds in North Canterbury, New Zealand, using structural mapping and geomorphic analysis. N. Z. J. Geol. Geophys. 46, 563–579.
Litchfield, N.J., Van Dissen, R., Sutherland, R., Barnes, P.M., Cox, S.C., Norris, R., Beavan, R.J., Langridge, R., Villamor, P., Berryman, K., Stirling, M., Nicol, A., Nodder, S., Lamarche, G., Barrell, D.J.A., Pettinga, J.R., Little, T., Pondard, N., Mountjoy, J.J., Clark, K., 2014. A model of active faulting in New Zealand. N. Z. J. Geol. Geophys. 57, 32–56.
Litchfield, N.J., Villamor, P., Dissen, R.J.V., Nicol, A., Barnes .A., P.M., Barrell, D.J., Pettinga, J.R., Langridge, R.M., Little, T.A., Mountjoy, J.J., Ries, W.F., Rowland, J., Fenton, C., Stirling, M.W., Kearse, J., Berryman, K.R., Cochran, U.A., Clark, K.J., Hemphill-Haley, M., Khajavi, N., Jones, K.E., Archibald, G., Upton, P., Asher, C., Benson, A., Cox, S.C., Gasston, C., Hale, D., Hall, B., Hatem, A.E., Heron, D.W., Howarth, J., Kane, T.J., Lamarche, G., Lawson, S., Lukovic, B., McColl, S.T., Madugo, C., Manousakis, J., Noble, D., Pedley, K., Sauer, K., Stahl, T., Strong, D.T., Townsend, D.B., Toy, V., Williams, J., Woelz, S., Zinke, R., 2018. Surface rupture of multiple crustal faults in the 2016 Mw 7.8 Kaikōura, New Zealand, earthquake. Bull. Seismol. Soc. Am. 108, 1496–1520.
Litchfield, N.J., Clark, K.J., Cochran, U.A., Palmer, A.S., Mountjoy, J., Mueller, C., Morgenstern, R., Berryman, K.R., McFadgen, B.G., Steele, R., Reitman, N., Howarth, J., Villamor, P., 2020. Marine terraces reveal complex Near-shore upper-plate faulting in the Northern Hikurangi Margin, New Zealand. Bull. Seismol. Soc. Am. 110 (2), 825–849. https://doi.org/10.1785/0120190208.
Little, T.A., Jones, A., 1998. Seven million years of strike-slip and related off-fault deformation, northeastern Marlborough fault system, South Island, New Zealand. Tectonics 17, 285–302.
Little, T.A., Van Dissen, R., Kearse, J., Norton, K., Benson, A., Wang, N., 2018. Kekerengu Fault, New Zealand: timing and size of late Holocene surface ruptures. Bull. Seismol. Soc. Am. 108, 1556–1572.
Longdill, P.C., Healy, T.R., Black, K.P., 2008. Transient wind-driven coastal upwelling on a shelf with varying width and orientation. N. Z. J. Mar. Freshw. Res. 42, 181–196.
Martinez Duran, P., Baillie, P., Carrillo, E., Duval, G., 2019. Geological Development of the Timor Orogen. Geological Society, London, Special Publications (SP490-2018-2120).
Mason, D.P.M., Little, T.A., Van Dissen, R.J., 2006. Rates of active faulting during late Quaternary fluvial terrace formation at Saxton River, Awatere fault, New Zealand. Geol. Soc. Am. Bull. 118, 1431–1446.
McCalpin, J.P., 1996. Tectonic geomorphology and Holocene paleoseismicity of the Molesworth section of the Awatere Fault, South Island, New Zealand. N. Z. J. Geol. Geophys. 39, 33–50.
McFadgen, B.G., 1987. Beach ridges, breakers and bones: late Holocene geology and archaeology of the Fyffe site, S49/46, Kaikōura Peninsula, New Zealand. J. R. Soc. N. Z. 17, 381–394.
Medwedeff, D.A., Suppe, J., 1997. Fault-related foldingmultibend fault-bend folding. J.

Struct. Geol. 19, 279–292.
Melnick, D., Bookhagen, B., Strecker, M.R., Echtler, H.P., 2009. Segmentation of megathrust rupture zones from fore-arc deformation patterns over hundreds to millions of years, Arauco peninsula, Chile. Journal of Geophysical Research: Solid Earth 114.
Mitrovica, J.X., Milne, G.A., 2002. On the origin of late Holocene sea-level highstands within equatorial ocean basins. Quat. Sci. Rev. 21, 2179–2190.
Mitrovica, J.X., Peltier, W.R., 1991. On postglacial geoid subsidence over the equatorial oceans. Journal of Geophysical Research: Solid Earth 96, 20053–20071.
Mountjoy, J.J., Barnes, P.M., 2011. Active Upper Plate Thrust Faulting in Regions of Low Plate Interface Coupling, Repeated Slow Slip Events, and Coastal Uplift: Example from the Hikurangi Margin, New Zealand. 12 (n/a-n/a).
Mouslopoulou, V., Walsh, J.J., Nicol, A., 2009. Fault displacement rates on a range of timescales. Earth Planet. Sci. Lett. 278, 186–197.
Mouslopoulou, V., Saltogianni, V., Nicol, A., Oncken, O., Begg, J., Babeyko, A., Cesca, S., Moreno, M., 2019. Breaking a subduction-termination from top to bottom: the large 2016 Kaikōura Earthquake, New Zealand. Earth Planet. Sci. Lett. 506, 221–230.
Muhs, D.R., Rockwell, T.K., Kennedy, G.L., 1992. Late quaternary uplift rates of marine terraces on the Pacific coast of North America, southern Oregon to Baja California Sur. Quat. Int. 15–16, 121–133.
Murray-Wallace, C.V., 2002. Pleistocene coastal stratigraphy, sea-level highstands and neotectonism of the southern Australian passive continental margin—a review. J. Quat. Sci. 17, 469–489.
Murray-Wallace, C.V., Belperio, A.P., Dosseto, A., Nicholas, W.A., Mitchell, C., Bourman, R.P., Eggins, S.M., Grün, R., 2016. Last interglacial (MIS 5e) sea-level determined from a tectonically stable, far-field location, Eyre Peninsula, southern Australia. Aust. J. Earth Sci. 63, 611–630.
Nicol, A., 1991. Structural Styles and Kinematics of Deformation on the Edge of the New Zealand Plate Boundary Zone, Mid-Waipara Region, North Canterbury. Department of Geological Sciences. University of Canterbury, Canterbury, New Zealand, pp. 153.
Nicol, A., Van Dissen, R., 2018. A 6000-year record of surface-rupturing paleoearthquakes on the Wairau Fault, New Zealand. N. Z. J. Geol. Geophys. 61, 341–358.
Nicol, A., Alloway, B.V., Tonkin, P.L., 1994. Rates of deformation, uplift and landscape development associated with active folding in the Waipara area of North Canterbury, New Zealand. Tectonics 13, 1327–1344.
Nicol, A., Walsh, J., Berryman, K., Villamor, P., 2006. Interdependence of Fault Displacement Rates and Paleoearthquakes in an Active Rift. 34. pp. 865.
Nicol, A., Khajavi, N., Pettinga, J.R., Fenton, C., Stahl, T., Bannister, S., Pedley, K., Hyland-Brook, N., Bushell, T., Hamling, I., Ristau, J., Noble, D., McColl, S.T., 2018. Preliminary geometry, displacement, and kinematics of fault ruptures in the Epicentral Region of the 2016 Mw 7.8 Kaikōura, New Zealand, earthquake. Bull. Seismol. Soc. Am. 108 (3B), 1521–1539. https://doi.org/10.1785/0120170329.
Normand, R., Simpson, G., Herman, F., Biswas, R.H., Bahroudi, A., Schneider, B., 2019. Dating and morpho-stratigraphy of uplifted marine terraces in the Makran subduction zone (Iran). Earth Surface Dynamics 7, 321–344.
Norris, R.J., Cooper, A.F., 2001. Late Quaternary slip rates and slip partitioning on the Alpine fault, New Zealand. J. Struct. Geol. 23, 507–520.
Oakley, D.O.S., Kaufman, D.S., Gardner, T.W., Fisher, D.M., Vanderleest, R.A., 2017. Quaternary marine terrace chronology, North Canterbury, New Zealand, using amino acid racemization and infrared-stimulated luminescence. Quat. Res. 87, 151–167.
Oakley, D.O.S., Fisher, D.M., Gardner, T.W., Stewart, M.K., 2018. Uplift rates of marine terraces as a constraint on fault-propagation fold kinematics: examples from the Hawkswood and Kate anticlines, North Canterbury, New Zealand. Tectonophysics 724–725, 195–219.
Ota, Y., Pillans, B., Berryman, K., Beu, A., Fujimori, T., Miyauchi, T., Berger, G., Beu, A.G., Climo, F.M., 1996. Pleistocene coastal terraces of Kaikōura Peninsula and the Marlborough coast, South Island, New Zealand. N. Z. J. Geol. Geophys. 39, 51–73.
Pettinga, J., Barnes, P., Bull, J., Gerring, P., Collins, J., 2019. The transpressive Mt Fyffe and seaward segments of the Hope Fault, Marlborough Fault System, New Zealand. Geophys. Res. Abstr. 21, 1.
Pico, T., Mitrovica, J.X., Ferrier, K.L., Braun, J., 2016. Global ice volume during MIS 3 inferred from a sea-level analysis of sedimentary core records in the Yellow River Delta. Quat. Sci. Rev. 152, 72–79.
Pico, T., Creveling, J.R., Mitrovica, J.X., 2017. Sea-level records from the U.S. mid-Atlantic constrain Laurentide Ice Sheet extent during Marine Isotope Stage 3. Nat. Commun. 8.
Pillans, B., 1990. Pleistocene marine terraces in New Zealand: a review. N. Z. J. Geol. Geophys. 33, 219–231.
Plafker, G., Rubin, M., 1978. Uplift history and earthquake recurrence as deduced from marine terraces on Middleton Island, Alaska. In: Isacks, B.L., Plafker, G. (Eds.), Proceedings of Conference VI, Methodology for Identifying Seismic Gaps and Soon-to-Break Gaps. USGS Open-File Report 78–943, 78–943 ed. United States Geological Survey, pp. 687–721.
Power, W., Clark, K., King, D.N., Borrero, J., Howarth, J., Lane, E.M., Goring, D., Goff, J., Chagué-Goff, C., Williams, J., Reid, C., Whittaker, C., Mueller, C., Williams, S., Hughes, M.W., Hoyle, J., Bind, J., Strong, D., Litchfield, N., Benson, A., 2017. Tsunami runup and tide-gauge observations from the 14 November 2016 M7.8 Kaikōura earthquake, New Zealand. Pure Appl. Geophys. 1–17.
Poynter, S., Goldberg, A., Hearty, D., 2013. Sedimentary and structural features of the Plio-Pleistocene Timor Accretionary Wedge, Timor-Leste. In: Moss, S.J., Keep, M. (Eds.), West Australian Basins Symposium 2013 Proceedings. Petroleum Exploration Society of Australia, Perth Convention Centre, Western Australia.
Quigley, M.C., Van Dissen, R., Litchfield, N., Villamor, P., Duffy, B., Barrell, D., Furlong, K., Stahl, T., Bilderback, E., Noble, D., 2012. Surface rupture during the 2010 M_W 7.1 Darfield (Canterbury) earthquake: implications for fault rupture dynamics and seismic-hazard analysis. Geology 40, 55–58.
Quigley, M.C., Lloret, A.J., Duffy, B., King, T., 2019. Physical and statistical behaviour of multi-fault earthquakes: Darfield earthquake case study, New Zealand. J. Geophys. Res. (Solid Earth) 124 (5), 4788–4810. https://doi.org/10.1029/2019JB017508. B017508.
Rattenbury, M.S., Townsend, D., Johnston, M.R., 2006. Geology of the Kaikōura Area, QMap. GNS Science, Lower Hutt, New Zealand. (p. Map + 79pp).
Reyners, M., Robinson, R., McGinty, P., 1997. Plate coupling in the northern South Island and southernmost North Island, New Zealand, as illuminated by earthquake focal mechanisms. J. Geophys. Res. 102, 15197–15210. https://doi.org/10.1029/97JB00973.
Rockwell, T.K., Keller, E.A., Dembroff, G.R., 1988. Quaternary rate of folding of the Ventura Avenue anticline, western Transverse Ranges, southern California. Geol. Soc. Am. Bull. 100, 850–858.
Rohling, E.J., Grant, K., Bolshaw, M., Roberts, A.P., Siddall, M., Hemleben, C., Kucera, M., 2009. Antarctic temperature and global sea level closely coupled over the past five glacial cycles. Nat. Geosci. 2, 500–504.
Rovere, A., Stocchi, P., Vacchi, M., 2016. Eustatic and relative sea level changes. Current Climate Change Reports 2, 221–231.
Salvaterra, A.D.S., Santos, R.F.D., Salaroli, A.B., Figueira, R.C.L., Mahiques, M.M.D., 2017. Evidence of an Marine Isotope Stage 3 transgression at the Baixada Santista, south-eastern Brazilian coast. Brazilian Journal of Geology 47, 693–702.
Saqab, M.M., Bourget, J., 2015. Structural style in a Young Flexure-induced oblique extensional system, North-Western Bonaparte basin, Australia. J. Struct. Geol. 77, 239–259.
Seeber, L., Sorlien, C.C., 2000. Listric thrusts in the western Transverse Ranges, California. Geol. Soc. Am. Bull. 112, 1067–1079.
Shulmeister, J., Soons, J.M., Berger, G.W., Harper, M., Holt, S., Moar, N., Carter, J.A., 1999. Environmental and sea-level changes on Banks Peninsula (Canterbury, New Zealand) through three glaciation–interglaciation cycles. Palaeogeogr. Palaeoclimatol. Palaeoecol. 152, 101–127.
Siddall, M., Rohling, E.J., Thompson, W.G., Waelbroeck, C., 2008. Marine isotope stage 3 sea level fluctuations: data synthesis and new outlook. Rev. Geophys. 46 (n/a-n/a).
Sieh, K., Jones, L., Hauksson, E., Hudnut, K., Eberhart-Phillips, D., Heaton, T., Hough, S., Hutton, K., Kanamori, H., Lilje, A., Lindvall, S., McGill, S.F., Mori, J., Rubin, C., Spotila, J.A., Stock, J., Thio, H.K., Treiman, J., Wernicke, B., Zachariasen, J., 1993. Near-field investigations of the Landers earthquake sequence, April to July 1992. Science 260, 171–176.
Simms, A.R., Dewitt, R., Rodriguez, A.B., Lambeck, K., Anderson, J.B., 2009. Revisiting marine isotope stage 3 and 5a (MIS3–5a) sea levels within the northwestern Gulf of Mexico. Glob. Planet. Chang. 66, 100–111.
Simons, M., Fialko, Y., Rivera, L., 2002. Coseismic deformation from the 1999 Mw 7.1 Hector Mine, California, earthquake as inferred from InSAR and GPS observations. Bull. Seismol. Soc. Am. 92, 1390–1402.
Sloss, C.R., Murray-Wallace, C.V., Jones, B.G., 2007. Holocene sea-level change on the southeast coast of Australia: a review. The Holocene 17, 999–1014.
Stephenson, W.J., Dickson, M.E., Denys, P.H., 2017. New insights on the relative contributions of coastal processes and tectonics to shore platform development following the Kaikōura earthquake. Earth Surf. Process. Landf. 42 (13), 2214–2220. https://doi.org/10.1002/esp.4176.
Stephenson, W.J., Kirk, R.M., Hemmingsen, M.A., 2019. Forty three years of micro-erosion meter monitoring of erosion rates on shore platforms at Kaikōura Peninsula, South Island, New Zealand. Geomorphology 344, 1–9.
Stirling, C.H., Esat, T.M., Lambeck, K., McCulloch, M.T., 1998. Timing and duration of the last interglacial: evidence for a restricted interval of widespread coral reef growth. Earth Planet. Sci. Lett. 160, 745–762.
Stirling, M.W., Litchfield, N., Villamor, P., Van Dissen, R., Nicol, A., Pettinga, J., Barnes, P., Langridge, R., Little, T., Barrell, D., Mountjoy, J., Ries, W.F., Rowland, J., Fenton, C., Hamling, I., Asher2, C., Barrier, A., Benson, A., Bischoff, A., Borella, J., Carne, R., Cochran, U.A., Cockroft, M., Cox, S.C., Duke, G., Fenton, F., Gasston, C., Grimshaw, C., Hale, D., Hall, B., Hao, K.X., Hatem, A., Hemphill-Haley, M., Heron, D.W., Howarth, J., Juniper, Z., Kane, T., Kearse, J., Khajavi, Lamarche, G., Lawson, S., Lukovic, B., Madugo, C., Manousakis, J., McColl, S., Noble, D., Pedley, K., Sauer, K., Stahll, T., Strong, D.T., Townsend, D.B., Toy, V., Villeneuve, M., Wandres, A., Williams, J., Woelz, S., Zinke, R., 2017. The Mw7. 8 2016 Kaikōura earthquake: surface fault rupture and seismic hazard context. Bull. N. Z. Soc. Earthq. Eng. 50, 73–84.
Suppe, J., 1983. Geometry and kinematics of fault-bend folding. Am. J. Sci. 283, 684–721.
Suppe, J., Medwedeff, D.A., 1990. Geometry and kinematics of fault-propagation folding. Eclogae Geol. Helv. 83, 409–454.
Suppe, J., Connors, C.D., Zhang, Y., 2004. Shear fault-bend folding. In: McClay, K.R. (Ed.), Thrust Tectonics and Hydrocarbon Systems: AAPG Memoir 82. American Association of Petroleum Geologists, pp. 303–323.
Tanabe, S., Saito, Y., Lan Vu, Q., Hanebuth, T.J.J., Lan Ngo, Q., Kitamura, A., 2006. Holocene evolution of the Song Hong (Red River) delta system, northern Vietnam. Sediment. Geol. 187, 29–61.
Ulrich, T., Gabriel, A.-A., Ampuero, J.-P., Xu, W., 2019. Dynamic viability of the 2016 Mw 7.8 Kaikōura earthquake cascade on weak crustal faults. Nat. Commun. 10, 1213.
van Dissen, R., Nicol, A., 2009. Mid-late Holocene paleoseismicity of the eastern Clarence Fault, Marlborough, New Zealand. N. Z. J. Geol. Geophys. 52, 195–208.
Van Dissen, R., Yeats, R.S., 1991. Hope fault, Jordan thrust, and uplift of the Seaward Kaikōura Range, New Zealand. Geology 19, 393.
Van Dissen, R.J., Sutherland, D.G., Bowers, R.J., Redwine, J.L., 2006. Forest burial by large rock avalanche in Miller Stream, Seaward Kaikōura Range, New Zealand, c. 1700 years ago. N. Z. J. Geol. Geophys. 49, 151–157.
VanderLeest, R.A., Fisher, D.M., Oakley, D.O.S., Gardner, T., 2017. Growth and seismic hazard of the Montserrat anticline in the North Canterbury fold and thrust belt, South

Island, New Zealand. J. Struct. Geol. 101, 1–14.
Wallace, L.M., Barnes, P., Beavan, J., Van Dissen, R., Litchfield, N., Mountjoy, J., Langridge, R., Lamarche, G., Pondard, N., 2012. The kinematics of a transition from subduction to strike-slip: an example from the Central New Zealand plate boundary. J. Geophys. Res. 117, B02405.
Walters, R.A., Barnes, P., Goff, J.R., 2006. Locally Generated Tsunami along the Kaikōura Coastal Margin: Part 1. Fault Ruptures. 40. pp. 1–16.
Williams, C.A., Eberhart-Phillips, D., Bannister, S., Barker, D.H.N., Henrys, S., Reyners, M., Sutherland, R., 2013. Revised interface geometry for the Hikurangi Subduction Zone, New Zealand. Seismol. Res. Lett. 84, 1066–1073.
Williams, J.N., Barrell, D.J.A., Stirling, M.W., Sauer, K.M., Duke, G.C., Hao, K.X., 2018. Surface rupture of the Hundalee Fault during the 2016 Mw 7.8 Kaikōura earthquake. Bull. Seismol. Soc. Am. 108, 1540–1555.
Woodroffe, S.A., Horton, B.P., 2005. Holocene sea-level changes in the Indo-Pacific. J. Asian Earth Sci. 25, 29–43.
Yousif, H.M.K., 1987. The Application of Remote Sensing to Geomorphological Neotectonic Mapping in North Canterbury. Department of Geological Sciences. University of Canterbury, Christchurch, New Zealand.